



HAL
open science

A multislope MUSCL method for vectorial reconstructions

Arthur Tételin, Clément Le Touze

► **To cite this version:**

Arthur Tételin, Clément Le Touze. A multislope MUSCL method for vectorial reconstructions. Journal of Computational Physics, 2024, 513, pp.113185. 10.1016/j.jcp.2024.113185 . hal-04684780

HAL Id: hal-04684780

<https://hal.science/hal-04684780v1>

Submitted on 3 Sep 2024

HAL is a multi-disciplinary open access archive for the deposit and dissemination of scientific research documents, whether they are published or not. The documents may come from teaching and research institutions in France or abroad, or from public or private research centers.

L'archive ouverte pluridisciplinaire **HAL**, est destinée au dépôt et à la diffusion de documents scientifiques de niveau recherche, publiés ou non, émanant des établissements d'enseignement et de recherche français ou étrangers, des laboratoires publics ou privés.

A multislope MUSCL method for vectorial reconstructions

Arthur Tételin^a, Clément Le Touze^{a,*}

^a*DMPE, ONERA, Université Paris Saclay, F-91123, Palaiseau, France*

Abstract

Variables interpolation is one of the key concepts of MUSCL schemes. Originally developed for one-dimensional frameworks, many improvements have been made over the last decades to extend these methods to general unstructured multi-dimensional meshes. It results that scalar interpolation in a finite volume cell-centered framework is already quite well understood. It is known that linear reconstructions have to be limited in order to prevent non-physical oscillations of the solutions while ensuring a spatial second-order accuracy for smooth solutions. This is done thanks to a limiting function which allows the reconstruction to satisfy a monotonicity property, which then ensure the stability of the scheme. Nevertheless, some difficulties arise when we try to extend this process to vectorial variables. Generally, vectorial reconstructions are done componentwise, but this process reveals to be frame-dependent and leads to a loss of precision due to false detection of extrema. In this paper, we present a new method dealing with vectorial reconstructions in a multislope MUSCL context.

Keywords: Cell-Centered Finite-Volume Methods, Unstructured Meshes, Multislope MUSCL Schemes, Vectorial Slope Limitation, Frame Invariance

1. Introduction

In the context of the cell-centered finite volume method applied to hyperbolic systems of conservation laws, it is usual to compute reconstructions of the variables in each control volume in order to improve the spatial accuracy of the convective fluxes approximation. To achieve this goal, van Leer developed at the end of the 70's an approach widely known today as the MUSCL approach [1–5]. Despite its lower accuracy [6] compared to ENO/WENO [7, 8] or Galerkin methods [9, Chap. 2], this class of method is very popular in industrial cell-centered CFD codes due to its higher efficiency. As it has been proved by Godunov and Bohachevsky [10], there is no high-order accurate scheme being both linear and not generating new extrema. To solve this issue, the idea of van Leer has been to introduce a limiting function whose aim is to limit the gradient of the variable in order to ensure some monotonicity criterion for the reconstructed variable [11, 12]. For one-dimensional schemes, this monotonicity criterion is designed so that the scheme satisfy a Total Variation Diminishing (TVD) property [13] which leads to the scheme stability. But for meshes of dimension two or higher, it has been proved that the TVD property and high order accuracy in space are incompatible [14]. Many studies have been published in order to ensure some stability for the scheme [15–17]. Today, several MUSCL schemes have been designed in order to deal with cells with any kind of polygonal shape on multidimensional meshes. These multidimensional schemes can be divided into two groups [18]: monoslope schemes computing a single gradient for each cell [19, 20], and multislope schemes computing a single directional gradient for every face of each cell [21–23].

All the studies on multidimensional grids mentioned above have been conducted for scalar variables. For vectorial variables, such as velocity, as far as the authors know, only very few studies have been made. In many codes, vectorial reconstructions mainly consist in a componentwise reconstruction. For instance,

*Corresponding author

Email address: `clement.le_touze[at]onera.fr` (Clément Le Touze)

this is the case of ONERA’s software CEDRE, dedicated to multi-physics problems in energetics on general unstructured meshes [24, 25]. Nevertheless, this kind of process turns out to be frame-dependent and leads to a loss of accuracy. In the literature, methods developed to solve this problem can be divided into two categories. The first one, developed by Luttwak and Falcovitz [26–28] has been originally designed for an Arbitrary Lagrangian-Eulerian framework. With a scalar conservation law, the variable satisfies a maximum principle in the form $\min_{j \in \mathcal{V}(i)} U_j \leq U_i^{n+1} \leq \max_{j \in \mathcal{V}(i)} U_j$, where $\mathcal{V}(i)$ is some neighborhood of the control volume K_i . For a vectorial conservation law, the extension of this maximum principle is a maximum principle componentwise, *whatever basis we choose*. In other words, the vector \mathbf{V}_i^{n+1} has to lie in the convex hull of vectors from a certain neighborhood. This convex hull has been called VIP (for *Vector Image Polygon / Polyhedron*) by Luttwak and Falcovitz and is the main element of their method. They indeed imposed on their reconstructed vector to lie within this area. Other works extended this method for other contexts, as Hoch and Labourasse [29] who extended the formalism on finite volume schemes, Velechovský et al. [30] who adapted it for problems with radial velocity, or Luttwak [28] who defined the much simpler bounding box concept to deal with many dimensional problems. Luttwak and Falcovitz [27] also used this method to define a scalar limitation. The second category has been initially developed by Maire [31, 32] in a monoslope context. It consists in defining a local basis in which all vectors will be limited componentwise. As the local basis is frame-independent, the limited componentwise vector is also frame-independent. This method has been used in many papers, each proposing different local bases [33–38]. All these methods present some advantages and drawbacks. The VIP method is the most natural extension of the monotonicity criterion in the vectorial case. But its major drawback is its CPU cost which makes it unsuitable for industrial CFD codes. Indeed, the VIP method requires to compute for each control volume a convex hull to determine if a reconstructed vector satisfies the monotonicity constraint or not. In industrial codes solving equations from fluid dynamics problems on arbitrary meshes, the computational cost of the VIP area can be really heavy. From this point of view, projections methods are simpler and have a lower computational cost than VIP methods. However, as the projections methods still involve a componentwise limiting procedure, they are prone to the same drawbacks as the classical componentwise methods (except from the frame dependency). This means in particular accuracy issues related to the detection of extrema for each component, as it will be explained in section 2.4.

For all the reasons mentioned above, we propose in this article a new reconstruction method for vectorial variables in the context of multislope MUSCL methods. This new method is based on an extension of the monotonicity constraint of the scalar case to a vectorial framework. In section 2, we recall the classical scalar multislope method. We also introduce the Limited- κ schemes, defined in order to avoid the use of the classical slope ratio r . We finish this section with a description of the issues arising with a componentwise reconstruction. In section 3, we present our strategy for vectorial reconstructions. We extend the Limited- κ -schemes introduced in section 2 to a vectorial framework, and we propose some vectorial limiting functions. Finally, numerical tests are performed in section 4 in order to assess the new vectorial method.

2. Multislope MUSCL scheme for scalar variables

In this section, we describe the multislope MUSCL scheme developed by Le Touze et al. [22], which is the basis of the vectorial reconstruction method we propose. It has been introduced to deal with the discretization of hyperbolic systems of conservation laws using the finite volume method on general unstructured meshes.

2.1. Finite volume discretization of hyperbolic conservation laws

We consider a computational domain Ω of dimension d . If, for $\mathbf{x} \in \mathbb{R}^d$, we note $\mathbf{Q} = \mathbf{Q}(\mathbf{x}, t)$ the vector of conserved variables, $\boldsymbol{\lambda} = \boldsymbol{\lambda}(\mathbf{x}, t)$ the velocity vector field, and \mathbf{f} the physical flux, then the system reads:

$$\frac{\partial \mathbf{Q}}{\partial t} + \nabla \cdot \mathbf{f}(\mathbf{Q}, \boldsymbol{\lambda}) = \mathbf{0}. \quad (1)$$

To get the finite volume scheme, we first discretize Ω in N_c non-overlapping cells denoted by K_i (with $|K_i|$ their volume), and which may have any kind of polygonal geometry in a 2- or 3-dimensional framework.

Each of these cells has a barycenter \mathbf{B}_i , and two adjacent cells are separated by a common face $S_{ij} = K_i \cap K_j$ (with $|S_{ij}|$ their surface area), whose barycenter is denoted by \mathbf{M}_{ij} . Let \mathbf{n}_{ij} stand for the unit normal vector of the face S_{ij} pointing outwards K_i , $\mathcal{V}(i)$ be the face neighborhood of the cell K_i , and $\mathcal{W}(i)$ its vertex neighborhood. We will sometimes use the notations $\bar{\mathcal{V}}(i)$ and $\bar{\mathcal{W}}(i)$ when we want to include K_i in these neighborhoods. In order to have the semi-discretized form of the scheme, we integrate over each cell K_i , and skipping the classical details of the finite volume method, we get the semi-discretized finite volume scheme:

$$\forall K_i \in \Omega, \quad \frac{d\mathbf{Q}_i(t)}{dt} = - \sum_{j \in \mathcal{V}(i)} \frac{|S_{ij}|}{|K_i|} \Phi_{ij}(\mathbf{Q}_{ij}(t), \mathbf{Q}_{ji}(t), \mathbf{n}_{ij}). \quad (2)$$

Here, $\mathbf{Q}_i(t)$ is by definition the mean value of $\mathbf{Q}(\mathbf{x}, t)$ in the cell K_i , which also approximates the value of $\mathbf{Q}(\mathbf{x}, t)$ at the barycenter \mathbf{B}_i with a second-order accuracy. Similarly, Φ_{ij} is the numerical flux function approximating the mean value of the physical flux at the face S_{ij} . To achieve a second-order accuracy, a MUSCL approach has been used, that is replacing $\mathbf{Q}_i(t)$ and $\mathbf{Q}_j(t)$ in the numerical flux by approximations $\mathbf{Q}_{ij}(t)$ and $\mathbf{Q}_{ji}(t)$ at the faces barycenters \mathbf{M}_{ij} . In this form, we still have to establish a time discretization. This is classically done by means of explicit Strong Stability Preserving Runge-Kutta (SSPRK) schemes, which are convex combinations of forward Euler steps [39]:

$$\frac{d\mathbf{Q}_i(t)}{dt} \approx \frac{\mathbf{Q}_i^{n+1} - \mathbf{Q}_i^n}{\Delta t}. \quad (3)$$

In the sections that follow, we will focus on the way variables are reconstructed at the faces centroids \mathbf{M}_{ij} . When dealing with systems of conservation equations, a crucial issue of the reconstruction process is the choice of the interpolated variables. This means for instance interpolating primitive variables rather than conserved quantities so as to preserve the positivity of physical variables like pressure or density. In this paper, we will especially focus on the way vectorial variables (like velocity for example) are reconstructed. To do so, we first need to recall the principles of the multislope method applied to scalar variables, which is the purpose of the next section.

2.2. Summary of the scalar multislope method: reconstruction procedure and properties

In order to describe the multislope reconstruction applied to scalar variables, we consider a simplified version of equation (1), namely a conservation law for a scalar quantity $u(\mathbf{x}, t)$ of the form:

$$\frac{\partial u(\mathbf{x}, t)}{\partial t} + \nabla \cdot (\boldsymbol{\lambda}(\mathbf{x})u(\mathbf{x}, t)) = 0, \quad (4)$$

According to the finite volume framework described above, this equation is discretized as:

$$U_i^{n+1} = U_i^n - \Delta t \sum_{j \in \mathcal{V}(i)} \frac{|S_{ij}|}{|K_i|} \Phi_{ij}(U_{ij}^n, U_{ji}^n). \quad (5)$$

If we also assume that the velocity field $\boldsymbol{\lambda}$ is such that $\nabla \cdot \boldsymbol{\lambda} = 0$, then we have a scalar advection equation for which any solution $u(\mathbf{x}, t)$ has to respect a maximum principle in the sense that

$$\forall t > t_0, \quad \forall \mathbf{x}_0 \in \Omega, \quad \min_{\mathbf{x} \in \Omega} u(\mathbf{x}, t_0) \leq u(\mathbf{x}_0, t) \leq \max_{\mathbf{x} \in \Omega} u(\mathbf{x}, t_0). \quad (6)$$

This maximum principle should be verified also by the discrete solution, in the sense that

$$\forall t^n > t_0, \quad \forall K_i \in \Omega, \quad \min_{K_j \in \Omega} U_j^n \leq U_i^{n+1} \leq \max_{K_j \in \Omega} U_j^n, \quad (7)$$

so as to ensure the stability of the scheme. To achieve this goal, it all depends on the way the reconstructions U_{ij} and U_{ji} are defined, in addition to a classical CFL criterion on the time step.

The multislope reconstruction algorithm for the scalar case has been introduced by Le Touze et al. [22]. We will only summarize here the main aspects of this method, so that an interested reader should refer to this article to get more details. All definitions introduced here are also illustrated in figure 1. The principle of the multislope MUSCL method is as follows: rather than computing a single limited gradient for the whole cell as in monoslope methods [18–20], dedicated scalar slopes are computed for each face S_{ij} of the cell. More precisely, two slopes are computed on the axis $\mathbf{B}_i \mathbf{M}_{ij}$: a forward slope p_{ij}^+ and a backward slope p_{ij}^- . Hence, introducing the well-known slope-limiting function φ [11, 12, 40–42], we can write the reconstruction as

$$U_{ij} = U_i + \|\mathbf{B}_i \mathbf{M}_{ij}\| p_{ij}^+ \varphi(r_{ij}, \eta_{ij}^-, \eta_{ij}^+), \quad r_{ij} = \frac{p_{ij}^-}{p_{ij}^+}, \quad \eta_{ij}^+ = \frac{\|\mathbf{B}_i \mathbf{H}_{ij}^+\|}{\|\mathbf{B}_i \mathbf{M}_{ij}\|}, \quad \eta_{ij}^- = \frac{\|\mathbf{B}_i \mathbf{H}_{ij}^-\|}{\|\mathbf{B}_i \mathbf{M}_{ij}\|}, \quad (8)$$

where r_{ij} is the slope ratio, while η_{ij}^+ and η_{ij}^- are two geometrical parameters. In what follows, we will assume that the mesh is such that the following property holds:

$$\boxed{\eta_{ij}^+ \geq 1, \quad \eta_{ij}^- \geq 1.} \quad (9)$$

This is a property that most meshes will naturally exhibit, otherwise it can still be enforced when selecting the neighbors in the reconstruction process. Interpolating U at both a forward point \mathbf{H}_{ij}^+ and a backward point \mathbf{H}_{ij}^- on the axis $\mathbf{B}_i \mathbf{M}_{ij}$ (see details in [22]), these two slopes can be expressed as:

$$p_{ij}^+ = \frac{U_{\mathbf{H}_{ij}^+} - U_i}{\|\mathbf{B}_i \mathbf{H}_{ij}^+\|}, \quad p_{ij}^- = \frac{U_i - U_{\mathbf{H}_{ij}^-}}{\|\mathbf{B}_i \mathbf{H}_{ij}^-\|}. \quad (10)$$

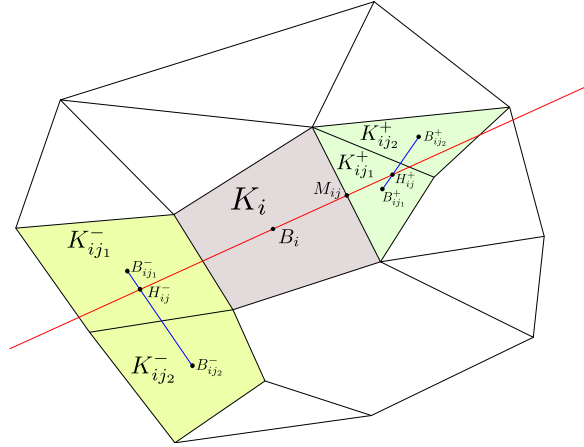


Figure 1: Multislope MUSCL scheme from Le Touze et al. [22] for two-dimensional meshes.

In the MUSCL framework, the slope limiting function φ plays an important role, as it ensures both accuracy and stability of the scheme. For the reconstructions to be second-order accurate in space, the limiting function has to satisfy

$$\varphi(r_{ij}) = 1. \quad (11)$$

Indeed, this property ensures that, if the variable u is linear in the vicinity of the cell K_i (i.e. $u(\mathbf{x}) = u(\mathbf{x}_0) + \nabla u|_i \cdot (\mathbf{x} - \mathbf{x}_0)$), then the reconstructed value U_{ij} at the point \mathbf{M}_{ij} will be exact. If the physical flux is linear and if we use an upwind numerical flux $\Phi_{ij}(U_{ij}, U_{ji}) = \max(0, \boldsymbol{\lambda} \cdot \mathbf{n}_{ij})U_{ij} + \min(0, \boldsymbol{\lambda} \cdot \mathbf{n}_{ij})U_{ji}$, then the method approximates the term $\nabla \cdot (\boldsymbol{\lambda} u)$ with a second-order accuracy. Generally, slope limiting functions are also built as convex combinations of Beam-Warming and Lax-Wendroff schemes [11, 21, 40–44], namely:

$$\boxed{\min(1, r_{ij}) \leq \varphi(r_{ij}) \leq \max(1, r_{ij}).} \quad (12)$$

Another property proved by Le Touze et al. [22] is that the scheme satisfies a discrete maximum principle similar to (7), but localized to the vertex neighborhood of the cell:

$$\forall K_i \in \Omega, \quad \min_{K_j \in \mathcal{W}(i)} U_j^n \leq U_i^{n+1} \leq \max_{K_j \in \mathcal{W}(i)} U_j^n, \quad (13)$$

implying the L^∞ stability of the scheme. Without going into details regarding the proof of Le Touze et al. [22], let us just recall that it results in two sufficient conditions, one is a classical CFL-like condition on the time step, the other one is a monotonicity condition imposed to the limiter function, which reads:

$$0 \leq \varphi(r_{ij}, \eta_{ij}^-, \eta_{ij}^+) \leq \max(0, \min(\eta_{ij}^- r_{ij}, \eta_{ij}^+)). \quad (14)$$

Both conditions (12) and (14) (respectively accounting for second-order and monotonicity) have to be combined, giving rise to the classical "second-order monotonicity area" for the limiter:

$$\max[0, \min(1, r_{ij})] \leq \varphi(r_{ij}, \eta_{ij}^-, \eta_{ij}^+) \leq \min[\max(0, \min(\eta_{ij}^- r_{ij}, \eta_{ij}^+)), \max(1, r_{ij})], \quad (15)$$

whose lower and upper bounds respectively define the Minmod and Superbee limiters. This is illustrated by the Sweby diagram in figure 3. Note that the monotonicity constraint (14) is written here as a condition on the limiter function φ , but it can be expressed under other equivalent forms as well (see next section). Also note that it has to be distinguished from the maximum principle (13). The monotonicity constraint is a condition imposed at the reconstruction level only, which happens to be a sufficient condition in order to get the maximum principle (13), and therefore the L^∞ -stability of the whole space-time scheme for the scalar advection equation.

2.3. Alternative formulations of the multislope reconstruction

In section 3, a new reconstruction method for vectorial variables will be introduced. It is based on an alternative way of defining reconstructions in the scalar case, which we will describe here. A first alternative definition of the reconstructions U_{ij} is based on the κ -scheme introduced by van Leer [4, 45]:

$$U_{ij} = U_i + \|\mathbf{B}_i \mathbf{M}_{ij}\| \left(\frac{1 + \kappa}{2} p_{ij}^+ + \frac{1 - \kappa}{2} p_{ij}^- \right), \quad \kappa \in [-1, 1]. \quad (16)$$

In this form, the reconstruction is linear and we have to introduce a limiting function. When defining limiting functions based on κ -schemes, it is usual to define them piecewise by combining the monotonicity constraint (14) and the κ -scheme [12, 42]. For instance, we can write the Monotonized Central limiter proposed by van Leer [4] (sometimes called MUSCL limiter), based on the value $\kappa = 0^1$:

$$\varphi^{MC}(r_{ij}, \eta_{ij}^-, \eta_{ij}^+) = \max \left[0, \min \left(\eta_{ij}^+, \frac{1 + r_{ij}}{2}, \eta_{ij}^- \right) \right], \quad (17)$$

or the Koren limiter [46], based on the value $\kappa = 1/3^2$:

$$\varphi^K(r_{ij}, \eta_{ij}^-, \eta_{ij}^+) = \max \left[0, \min \left(\eta_{ij}^+, \frac{2 + r_{ij}}{3}, \eta_{ij}^- \right) \right]. \quad (18)$$

In our alternative formulation of the reconstructions, we will follow another approach. Rather than introducing the κ -scheme in a piecewise function, we will replace the scalar κ by a function $\kappa_{ij} = \kappa(p_{ij}^+, p_{ij}^-, \eta_{ij}^+, \eta_{ij}^-)$

¹A κ -scheme based on the value $\kappa = 0$ corresponds to the standard second-order central scheme.

²This limiter provides a third-order accuracy on regular one-dimensional meshes. However, on multi-dimensional or unstructured meshes, it loses its third-order accuracy as stated in [12].

with slopes (or their ratio r_{ij}) and geometrical parameters as arguments. This function is called the Limited- κ (LK) function. We also introduce a sensor function σ_{ij} based on the slopes sign, whose aim is to make the reconstruction degenerate to a first-order accuracy at extrema:

$$\sigma_{ij} = \begin{cases} 1 & \text{if } p_{ij}^+ p_{ij}^- > 0 \\ 0 & \text{if } p_{ij}^+ p_{ij}^- \leq 0 \end{cases}. \quad (19)$$

155 When using these functions, the Limited κ -scheme (LKS) reads:

$$U_{ij} = U_i + \|\mathbf{B}_i \mathbf{M}_{ij}\| \sigma_{ij} \left(\frac{1 + \kappa_{ij}}{2} p_{ij}^+ + \frac{1 - \kappa_{ij}}{2} p_{ij}^- \right). \quad (20)$$

The link between the LK function and the slope-limiting function is quite obvious, as:

$$p_{ij}^+ \varphi(r_{ij}, \eta_{ij}^-, \eta_{ij}^+) = \sigma_{ij} \left(\frac{1 + \kappa_{ij}}{2} p_{ij}^+ + \frac{1 - \kappa_{ij}}{2} p_{ij}^- \right). \quad (21)$$

For $r_{ij} > 0$ and $r_{ij} \neq 1^3$, it is equivalent to

$$\kappa_{ij} = \frac{2\varphi(r_{ij}, \eta_{ij}^-, \eta_{ij}^+) - 1 - r_{ij}}{1 - r_{ij}} = 1 - 2 \frac{1 - \varphi(r_{ij}, \eta_{ij}^-, \eta_{ij}^+)}{1 - r_{ij}}. \quad (22)$$

Hence, all classical limiters can be expressed as LK functions. For example, the Monotonized Central limiter (17) reads in this form:

$$\kappa^{MC}(r_{ij}, \eta_{ij}^+, \eta_{ij}^-) = \frac{(2\eta_{ij}^- - 1)r_{ij} - 1}{1 - r_{ij}} \mathbb{I}_{[0, (2\eta_{ij}^- - 1)^{-1}]}(r_{ij}) + \frac{2\eta_{ij}^+ - 1 - r_{ij}}{1 - r_{ij}} \mathbb{I}_{[2\eta_{ij}^+ - 1, \infty]}(r_{ij}), \quad (23)$$

160 with $\mathbb{I}_A(r_{ij})$ an indicator function defined such that

$$\mathbb{I}_A(r_{ij}) = \begin{cases} 1 & \text{if } r_{ij} \in A \\ 0 & \text{if } r_{ij} \notin A \end{cases}. \quad (24)$$

From relation (22) and the monotonicity constraint on the limiter (14), it is possible to deduce an interval for the Limited- κ function such that the reconstruction is limited adequately for the scheme stability. If $\forall r_{ij} > 0, r_{ij} \neq 1$, we introduce

$$\kappa^-(r_{ij}, \eta_{ij}^-) = \kappa_{ij}^- = \frac{2\eta_{ij}^- r_{ij} - 1 - r_{ij}}{1 - r_{ij}}, \quad \kappa^+(r_{ij}, \eta_{ij}^+) = \kappa_{ij}^+ = \frac{2\eta_{ij}^+ - 1 - r_{ij}}{1 - r_{ij}}, \quad (25)$$

165 namely the monotonicity bounding κ -functions, respectively corresponding to $\varphi_{ij} = \eta_{ij}^- r_{ij}$ and $\varphi_{ij} = \eta_{ij}^+$, then the numerical scheme with reconstructions under the LKS form (20) is stable if the LK function satisfies:

$$\kappa_{ij} \in [-1, 1] \setminus [\min(\kappa_{ij}^-, \kappa_{ij}^+), \max(\kappa_{ij}^-, \kappa_{ij}^+)]. \quad (26)$$

Both κ_{ij}^- and κ_{ij}^+ blow up when r_{ij} is close to 1 (and are undefined when $r_{ij} = 1$). But this does not matter since in this area any suitable scheme is bounded by the linear second-order schemes obtained with $\kappa = 1$ and $\kappa = -1$. This is illustrated in figure 3b where all four bounding κ functions are plotted versus the slope

³Note that κ_{ij} is undefined when $r_{ij} = 1$, but this is not a problem. It only means that all κ -schemes are equivalent in the linear case $p_{ij}^- = p_{ij}^+$, i.e when the limiter function can only take the value $\varphi_{ij}(1) = 1$. When r_{ij} is close to 1, the relation (12) also implies that $|1 - \varphi_{ij}| \leq |1 - r_{ij}|$, thereby ensuring that κ_{ij} does not blow up.

ratio (in log scale). Let us now consider another formulation of the reconstruction. Let U_{ij}^- and U_{ij}^+ be the linear κ -schemes (16) respectively obtained using $\kappa = -1$ and $\kappa = 1$:

$$\begin{cases} U_{ij}^- \triangleq U_i + \|\mathbf{B}_i \mathbf{M}_{ij}\| p_{ij}^- = U_i + \frac{1}{\eta_{ij}^-} (U_i - U_{\mathbf{H}_{ij}^-}) \\ U_{ij}^+ \triangleq U_i + \|\mathbf{B}_i \mathbf{M}_{ij}\| p_{ij}^+ = U_i + \frac{1}{\eta_{ij}^+} (U_{\mathbf{H}_{ij}^+} - U_i) \end{cases}, \quad (27)$$

and let U_{ij}^{--} and U_{ij}^{++} be the monotonicity bounds from (14) expressed on U_{ij} :

$$\begin{cases} U_{ij}^{--} \triangleq U_i + (U_i - U_{\mathbf{H}_{ij}^-}) = 2U_i - U_{\mathbf{H}_{ij}^-} \\ U_{ij}^{++} \triangleq U_i + (U_{\mathbf{H}_{ij}^+} - U_i) = U_{\mathbf{H}_{ij}^+} \end{cases}. \quad (28)$$

Thus the "second order monotonicity area" can be defined also as the set of all reconstructions U_{ij} being a convex combination of U_{ij}^- and U_{ij}^+ , namely:

$$U_{ij} - U_i = \sigma_{ij} \left[\frac{1+\kappa}{2} (U_{ij}^+ - U_i) + \frac{1-\kappa}{2} (U_{ij}^- - U_i) \right], \quad \kappa \in [-1, 1], \quad (29)$$

provided that they are bounded by the monotonicity bounds U_{ij}^{--} and U_{ij}^{++} in the following way:

$$|U_{ij} - U_i| \leq \min (|U_{ij}^{--} - U_i|, |U_{ij}^{++} - U_i|). \quad (30)$$

Finally, we can sum up all the alternative (but equivalent) formulations of the "second-order monotonicity area" as described in figure 2 and illustrated in figure 3. The main advantage of the LKS and " $|U_{ij} - U_i|$ bounding" formulations is that they do not directly involve the slope ratio r_{ij} , which will simplify the extension to the vectorial case (see section 3).

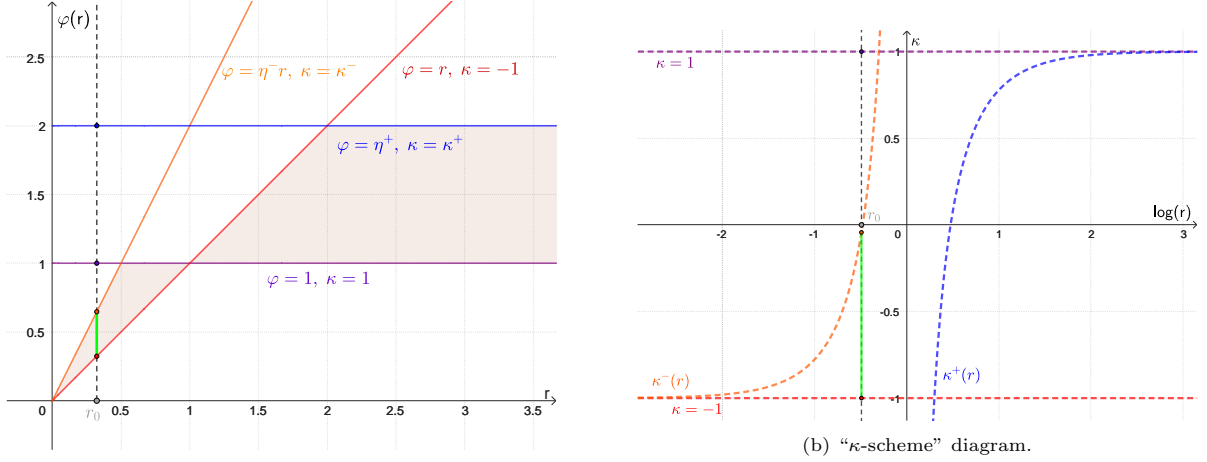
Limiter function formulation	
$U_{ij} = U_i + \ \mathbf{B}_i \mathbf{M}_{ij}\ p_{ij}^+ \varphi(r_{ij}, \eta_{ij}^-, \eta_{ij}^+)$ $\max[0, \min(1, r_{ij})] \leq \varphi(r_{ij}, \eta_{ij}^-, \eta_{ij}^+) \leq \min[\min(\eta_{ij}^- r_{ij}, \eta_{ij}^+), \max(1, r_{ij})]$	
$U_{ij} = U_i + \ \mathbf{B}_i \mathbf{M}_{ij}\ \sigma_{ij} \left(\frac{1+\kappa_{ij}}{2} p_{ij}^+ + \frac{1-\kappa_{ij}}{2} p_{ij}^- \right)$ $\kappa_{ij} \in [-1, 1] \setminus [\min(\kappa_{ij}^-, \kappa_{ij}^+), \max(\kappa_{ij}^-, \kappa_{ij}^+)]$	$U_{ij} - U_i = \sigma_{ij} \left[\frac{1+\kappa}{2} (U_{ij}^+ - U_i) + \frac{1-\kappa}{2} (U_{ij}^- - U_i) \right], \quad \kappa \in [-1, 1],$ $ U_{ij} - U_i \leq \min (U_{ij}^{--} - U_i , U_{ij}^{++} - U_i)$
Limited κ -scheme (LKS) formulation	" $U_{ij} - U_i$ " bounding formulation

Figure 2: Alternative but equivalent formulations of the "second-order monotonicity area" in the scalar case.

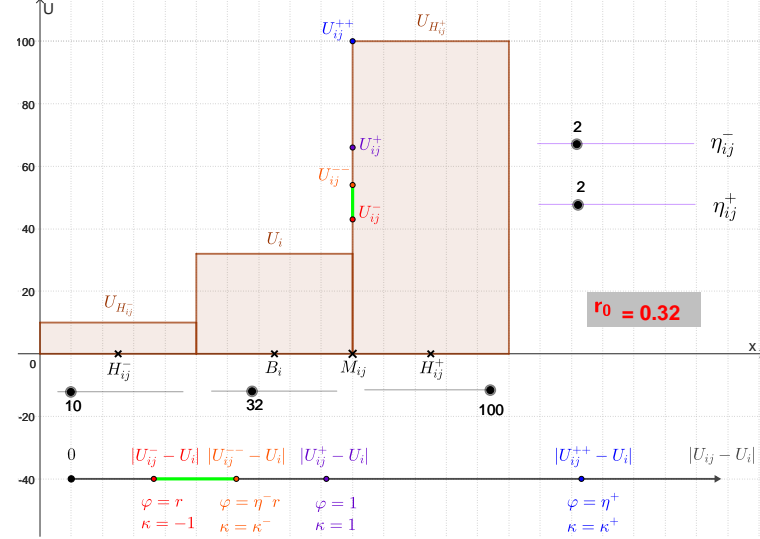
2.4. Componentwise reconstructions for vectorial variables

When dealing with vectorial variables, the straightforward approach is to apply the scalar reconstruction procedure to each component independently, which we refer to as the componentwise reconstruction. However, as already noticed in the literature [26, 31] this approach is frame-dependent (see the example given in Appendix A). In fact, we can precise this behavior of componentwise reconstructions by examining the slopes. First, notice that whether the vectorial quantities to be reconstructed are defined in a 2D or 3D space, the reconstruction procedure can always be tackled in the 2D plane generated by the slope vectors \mathbf{p}_{ij}^- and \mathbf{p}_{ij}^+ . This is an interesting feature that will be used when designing a vectorial approach in section 3. Now if the slopes are non-vanishing, then we can state the following results (a summary is provided in table 1 and proofs are given in Appendix B):

1. If slopes are colinear, then we have the only totally frame-independent componentwise reconstruction, since it is actually just a scalar problem. By the way, reverting to the scalar case when slopes are colinear is a natural behavior that we would like to preserve when we design a new vectorial scheme in section 3.



(a) Sweby's diagram.



(c) “ $|U_{ij} - U_i|$ bounding” representation.

Figure 3: Several representations of the “second-order monotonicity” area for the scalar case (example taken with a value $r = 0.32$). This figure is extracted from a Geogebra applet available online [47], and allows to visualize the evolution of the “second-order stability” area when moving the cursors $U_{H_{ij}^-}$, U_i , $U_{H_{ij}^+}$, η_{ij}^- et η_{ij}^+ .

2. If slopes are noncolinear, then we have several cases depending on the scalar product $\mathbf{p}_{ij}^+ \cdot \mathbf{p}_{ij}^-$:

- 195 (a) Case $\mathbf{p}_{ij}^+ \cdot \mathbf{p}_{ij}^- > 0$:
- i. For any basis, there is always at least one component reconstructed at second-order accuracy.
 - ii. There exists at least one basis in which at least one component is first-order accurate.
 - iii. There exists at least one basis in which all components are second-order accurate.
- 200 (b) Case $\mathbf{p}_{ij}^+ \cdot \mathbf{p}_{ij}^- < 0$:
- i. For any basis, there is always at least one component reconstructed at first-order accuracy.
 - ii. There exists at least one basis in which at least one component is second-order accurate.
 - iii. There exists at least one basis in which all components are first-order accurate.
- 205 (c) Case $\mathbf{p}_{ij}^+ \cdot \mathbf{p}_{ij}^- = 0$:
- i. For any orthonormal basis \mathcal{B}_0 with at least one component colinear with one of the vectorial slope, all components will be reconstructed with a first-order accuracy.



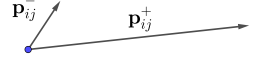
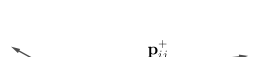
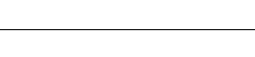
Illustration	Configuration of the slopes	Properties
	$\mathbf{p}_{ij}^+ = \alpha \mathbf{p}_{ij}^-$ and $\mathbf{p}_{ij}^+ \cdot \mathbf{p}_{ij}^- > 0$	$\forall \mathcal{B} \in \mathbb{R}^d, \forall k, (\mathbf{p}_{ij}^+)_k (\mathbf{p}_{ij}^-)_k \geq 0$
	$\mathbf{p}_{ij}^+ = \alpha \mathbf{p}_{ij}^-$ and $\mathbf{p}_{ij}^+ \cdot \mathbf{p}_{ij}^- \leq 0$	$\forall \mathcal{B} \in \mathbb{R}^d, \forall k, (\mathbf{p}_{ij}^+)_k (\mathbf{p}_{ij}^-)_k \leq 0$
	$\mathbf{p}_{ij}^+ \neq \alpha \mathbf{p}_{ij}^-$ and $\mathbf{p}_{ij}^+ \cdot \mathbf{p}_{ij}^- > 0$	$\forall \mathcal{B} \in \mathbb{R}^d, \exists k, (\mathbf{p}_{ij}^+)_k (\mathbf{p}_{ij}^-)_k > 0$ $\exists \mathcal{B} \in \mathbb{R}^d, \exists k, (\mathbf{p}_{ij}^+)_k (\mathbf{p}_{ij}^-)_k < 0$ $\exists \mathcal{B} \in \mathbb{R}^d, \forall k, (\mathbf{p}_{ij}^+)_k (\mathbf{p}_{ij}^-)_k \geq 0$
	$\mathbf{p}_{ij}^+ \neq \alpha \mathbf{p}_{ij}^-$ and $\mathbf{p}_{ij}^+ \cdot \mathbf{p}_{ij}^- < 0$	$\forall \mathcal{B} \in \mathbb{R}^d, \exists k, (\mathbf{p}_{ij}^+)_k (\mathbf{p}_{ij}^-)_k < 0$ $\exists \mathcal{B} \in \mathbb{R}^d, \exists k, (\mathbf{p}_{ij}^+)_k (\mathbf{p}_{ij}^-)_k > 0$ $\exists \mathcal{B} \in \mathbb{R}^d, \forall k, (\mathbf{p}_{ij}^+)_k (\mathbf{p}_{ij}^-)_k \leq 0$
	$\mathbf{p}_{ij}^+ \neq \alpha \mathbf{p}_{ij}^-$ and $\mathbf{p}_{ij}^+ \cdot \mathbf{p}_{ij}^- = 0$	$\exists \mathcal{B}_0 \in \mathbb{R}^d, \forall k, (\mathbf{p}_{ij}^+)_k (\mathbf{p}_{ij}^-)_k = 0$ $\forall \mathcal{B} \neq \mathcal{B}_0, \exists k, (\mathbf{p}_{ij}^+)_k (\mathbf{p}_{ij}^-)_k > 0$ $\forall \mathcal{B} \neq \mathcal{B}_0, \exists k, (\mathbf{p}_{ij}^+)_k (\mathbf{p}_{ij}^-)_k < 0$

Table 1: Summary of the properties of the componentwise reconstruction. When the product of the forward and backward slopes for a given component is nonpositive, then the component is reconstructed only with a first-order accuracy.

- ii. For all other bases, there is always one component reconstructed with a second-order accuracy, and one component reconstructed with a first-order accuracy.

These properties illustrate the issue with the componentwise reconstruction. While we expect all components to be reconstructed with the same accuracy, the slope limiting function can falsely detect some extrema for some components. When this happens, the reconstruction degenerates to first-order for that particular component, which degrades the overall precision of the scheme. As the accuracy of the solution depends only on the basis chosen to express the vectors, the method is thus frame-dependent, meaning that changing the basis changes the solution. This is a problem for the reliability of the simulations of physical systems, whose governing equations are supposed to exhibit a Galilean invariance, such as the Euler equations. This can even lead to practical problems in CFD simulations, for example with conservation issues when dealing with rotationally periodic boundary conditions (see the numerical test of section 4.2).

As detailed in the introduction, this issue has been studied in the literature, but none of the proposed solutions is entirely satisfactory. Moreover, the accuracy problem highlighted in this section still occurs in the projection methods [31–38], as they are not really vectorial, meaning that some vectors can still be reconstructed with a different order for each component. For all these reasons, we propose in the next section a new reconstruction method for vectorial variables, which we want to respect the following properties: frame-invariance, accuracy preserving, ensuring the stability of the scheme, low computational cost, reducing to a scalar method when slopes are colinear.

3. A new multislope MUSCL method for vectorial variables

3.1. Strategy for the reconstruction of vectorial variables

In order to introduce our strategy regarding the reconstruction of vectorial variables, let us consider the natural extension of the scalar framework used in section 2.2. Starting with the conservation law for a vectorial quantity \mathbf{v} , if we consider a linear physical flux $\mathbf{f}(\mathbf{v}) = \boldsymbol{\lambda} \otimes \mathbf{v}$, and if we assume a time-independent

velocity field such that $\nabla \cdot \boldsymbol{\lambda} = 0$, then we get the vectorial advection equation:

$$\frac{\partial \mathbf{v}}{\partial t} + (\boldsymbol{\lambda} \cdot \nabla) \mathbf{v} = \mathbf{0}, \quad (31)$$

with $(\boldsymbol{\lambda} \cdot \nabla)$ defined as:

$$(\boldsymbol{\lambda} \cdot \nabla) = \lambda_x \frac{\partial}{\partial x} + \lambda_y \frac{\partial}{\partial y} + \lambda_z \frac{\partial}{\partial z}. \quad (32)$$

As in the scalar case, this equation is discretized according to the finite volume framework described in section 2.1:

$$\mathbf{V}_i^{n+1} = \mathbf{V}_i^n - \Delta t \sum_{j \in \mathcal{V}(i)} \frac{|S_{ij}|}{|K_i|} \Phi_{ij}(\mathbf{V}_{ij}^n, \mathbf{V}_{ji}^n). \quad (33)$$

Like in the scalar case there exists a maximum principle on $\mathbf{v}(\mathbf{x}, t)$ in the sense that each of its components satisfies a maximum principle **whatever the basis considered**:

$$\forall t > t_0, \forall \mathbf{x}_0 \in \Omega, \forall k \in \{1 \cdots d\}, \quad \min_{\mathbf{x} \in \Omega} v_k(\mathbf{x}, t_0) \leq v_k(\mathbf{x}_0, t) \leq \max_{\mathbf{x} \in \Omega} v_k(\mathbf{x}, t_0), \quad (34)$$

where v_k is the k -th component of vector \mathbf{v} in any given basis. In other words, this means that each vector has to be in the convex hull spanned by the vector field at time t_0 :

$$\forall t > t_0, \forall \mathbf{x}_0 \in \Omega, \quad \mathbf{v}(\mathbf{x}_0, t) \in \text{Conv}(\{\mathbf{v}(\mathbf{x}, t_0) \mid \mathbf{x} \in \Omega\}), \quad (35)$$

which is the vectorial extension of the maximum principle (6) in the scalar case. By extension there also exists a maximum principle on the L^2 norm of the vectors, which reads:

$$\forall t > t_0, \forall \mathbf{x}_0 \in \Omega, \quad \|\mathbf{v}(\mathbf{x}_0, t)\|_2 \leq \max_{\mathbf{x} \in \Omega} \|\mathbf{v}(\mathbf{x}, t_0)\|_2. \quad (36)$$

Ideally, these properties should be also verified at the discrete level with a good vectorial reconstruction method. This would mean a discrete maximum principle for \mathbf{V}_i^{n+1} , typically with respect to the vertex-neighborhood $\mathcal{W}(i)$ of the local cell K_i , namely:

$$\forall t^n > t_0, \forall K_i \in \Omega, \quad \mathbf{V}_i^{n+1} \in \text{Conv}(\{\mathbf{V}_j^n \mid K_j \in \bar{\mathcal{W}}(i)\}), \quad (37)$$

as well as

$$\forall t^n > t_0, \forall K_i \in \Omega, \quad \|\mathbf{V}_i^{n+1}\|_2 \leq \max_{K_j \in \bar{\mathcal{W}}(i)} \|\mathbf{V}_j^n\|_2. \quad (38)$$

Like in the scalar case, this would automatically imply the stability of the overall space-time scheme. However the approach undertaken below is not primarily designed for this purpose. It rather consists in extending the monotonicity properties of the scalar reconstructions U_{ij} to the vectorial ones \mathbf{V}_{ij} , in a way that is frame-independent (not operating on individual components but on the whole vector), does not lead to a loss of accuracy due to false detection of extrema, and which remains compact (i.e localized to the three-point stencil $(\mathbf{H}_{ij}^-, \mathbf{B}_i, \mathbf{H}_{ij}^+)$) to preserve the computational cost. Even though it turns out that these extended monotonicity properties are not sufficient conditions to prove any maximum principle for \mathbf{V}_i^{n+1} (unlike the scalar case), they are still expected to be a solid empirical tool to get the stability in practice. Of course, this will then have to be assessed with numerical tests, which will be the purpose of section 4.

Remark 1. With componentwise vectorial reconstructions, we only get a scalar maximum principle on each individual component, which means that (37) does not hold. Indeed, one cannot guarantee that \mathbf{V}_i^{n+1} will lie in the convex hull, but only in the frame-dependent bounding box generated by the extremal values of the components, as illustrated in figure 4. This is enough though to prove the L^∞ -stability because this bounding box is time-invariant. But interestingly, this means that the discrete maximum principle on the norm (38) does not hold either (see figure 4), which can lead to surprising results in practice (see section 4.1 for an illustration).

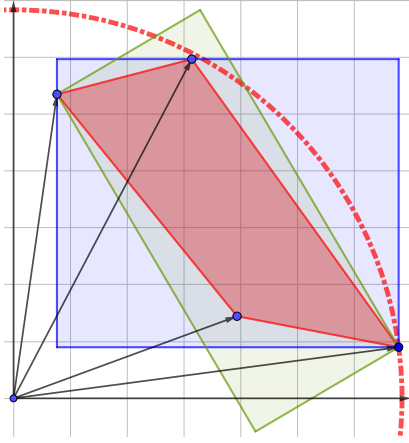


Figure 4: Illustration of the maximum principle in the vectorial case. A maximum principle on each individual component only results in a frame-dependent box (blue). The natural extension of the scalar maximum principle is the convex hull, i.e. the intersection of all the possible boxes whatever the basis considered (in red). The green box corresponds to a bounding box in some other random basis. The componentwise maximum principle does not imply the maximum principle on the norm as \mathbf{V}_i^{n+1} can lie inside a given box but outside the circle defined by the red dashed line.

3.2. Definition of the multislope vectorial reconstructions

260 In a similar way as in the scalar case, let us define the vectorial multislope reconstruction \mathbf{V}_{ij} as:

$$\mathbf{V}_{ij} = \mathbf{V}_i + \|\mathbf{B}_i \mathbf{M}_{ij}\| \mathbf{p}_{ij}. \quad (39)$$

265 Here $\mathbf{p}_{ij} = f(\mathbf{p}_{ij}^+, \mathbf{p}_{ij}^-, \eta_{ij}^+, \eta_{ij}^-)$ is the effective limited slope vector, which is a function of both \mathbf{p}_{ij}^- and \mathbf{p}_{ij}^+ , respectively the backward and forward slope vectors, (computed in the same way as their scalar counterparts), and of the geometrical parameters η_{ij}^- and η_{ij}^+ . In the scalar case we simply had $p_{ij} = \varphi(r_{ij})p_{ij}^+$. But difficulties arise with this form in the vectorial case, because the slope ratio r_{ij} cannot be easily defined anymore. Here comes the purpose of the LKS formulation introduced in the scalar case (see relation (20) of section 2.3). Indeed, the LKS formulation for vectorial variables can be easily expressed as:

$$\mathbf{p}_{ij} = \frac{\mathbf{V}_{ij} - \mathbf{V}_i}{\|\mathbf{B}_i \mathbf{M}_{ij}\|} = \sigma_{ij} \left(\frac{1 + \kappa_{ij}}{2} \mathbf{p}_{ij}^+ + \frac{1 - \kappa_{ij}}{2} \mathbf{p}_{ij}^- \right), \quad (40)$$

with $\kappa_{ij} = \kappa(\mathbf{p}_{ij}^+, \mathbf{p}_{ij}^-, \eta_{ij}^+, \eta_{ij}^-) \in [-1, 1]$ a vectorial limited- κ (VLK) function. Besides, σ_{ij} is a sensor function accounting for vectorial extrema, which can be defined based on the scalar analysis of section 2.4 as:

$$\sigma_{ij} = \begin{cases} 1 & \text{if } \mathbf{p}_{ij}^+ \cdot \mathbf{p}_{ij}^- > 0 \\ 0 & \text{if } \mathbf{p}_{ij}^+ \cdot \mathbf{p}_{ij}^- \leq 0 \end{cases}. \quad (41)$$

270 This definition of σ_{ij} leads to a natural geometrical interpretation of extrema when variables are vectors. If we consider the three vectors $(\mathbf{V}_{\mathbf{H}_{ij}^-}, \mathbf{V}_i, \mathbf{V}_{\mathbf{H}_{ij}^+})$ from the local three-point stencil $(\mathbf{H}_{ij}^-, \mathbf{B}_i, \mathbf{H}_{ij}^+)$, then \mathbf{V}_i is an extremum if the angle between the two vectorial slopes is greater than $\pi/2$ (see Figure 5). As κ_{ij} has a unique value for all components, the method is frame-invariant and potentially second-order accurate for all components. Now, we have to determine κ_{ij} depending on the slopes \mathbf{p}_{ij}^+ and \mathbf{p}_{ij}^- , in a way that extends the monotonicity properties of the scalar case.

275 To start with, and like in the scalar case (see relation (27)), let \mathbf{V}_{ij}^- and \mathbf{V}_{ij}^+ be the linear κ -schemes respectively obtained using $\kappa = -1$ and $\kappa = 1$:

$$\begin{cases} \mathbf{V}_{ij}^- \triangleq \mathbf{V}_i + \|\mathbf{B}_i \mathbf{M}_{ij}\| \mathbf{p}_{ij}^- = \mathbf{V}_i + \frac{1}{\eta_{ij}^-} (\mathbf{V}_i - \mathbf{V}_{\mathbf{H}_{ij}^-}) \\ \mathbf{V}_{ij}^+ \triangleq \mathbf{V}_i + \|\mathbf{B}_i \mathbf{M}_{ij}\| \mathbf{p}_{ij}^+ = \mathbf{V}_i + \frac{1}{\eta_{ij}^+} (\mathbf{V}_{\mathbf{H}_{ij}^+} - \mathbf{V}_i) \end{cases}, \quad (42)$$

and let \mathbf{V}_{ij}^{--} and \mathbf{V}_{ij}^{++} be the monotonicity bounds similar to relation (28):

$$\begin{cases} \mathbf{V}_{ij}^{--} \triangleq \mathbf{V}_i + \left(\mathbf{V}_i - \mathbf{V}_{\mathbf{H}_{ij}^-} \right) & = 2\mathbf{V}_i - \mathbf{V}_{\mathbf{H}_{ij}^-} \\ \mathbf{V}_{ij}^{++} \triangleq \mathbf{V}_i + \left(\mathbf{V}_{\mathbf{H}_{ij}^+} - \mathbf{V}_i \right) & = \mathbf{V}_{\mathbf{H}_{ij}^+} \end{cases} \quad (43)$$

Using these vectors, we can extend the "U_{ij} - U_i bounding" formulation of the "scalar second-order monotonicity area" (see relations (29) and (30), or figure 2). The "vectorial second-order monotonicity area" is thus defined as the set of all the reconstructions \mathbf{V}_{ij} that are a convex combination of \mathbf{V}_{ij}^- and \mathbf{V}_{ij}^+ , provided that they are bounded by the monotonicity bounds \mathbf{V}_{ij}^{--} and \mathbf{V}_{ij}^{++} in the following sense:

$$\begin{aligned} \mathbf{V}_{ij} - \mathbf{V}_i &= \sigma_{ij} \left[\frac{1+\kappa}{2} (\mathbf{V}_{ij}^+ - \mathbf{V}_i) + \frac{1-\kappa}{2} (\mathbf{V}_{ij}^- - \mathbf{V}_i) \right], \quad \kappa \in [-1, 1], \\ \|\mathbf{V}_{ij} - \mathbf{V}_i\| &\leq \min \left(\|\mathbf{V}_{ij}^{--} - \mathbf{V}_i\|, \|\mathbf{V}_{ij}^{++} - \mathbf{V}_i\| \right). \end{aligned} \quad (44)$$

Note that the bounding property hence operates on the norm of the effective slope, which can be expressed also as:

$$\|\mathbf{p}_{ij}\| \leq \sigma_{ij} \min \left(\eta_{ij}^- \|\mathbf{p}_{ij}^-\|, \eta_{ij}^+ \|\mathbf{p}_{ij}^+\| \right). \quad (45)$$

Now it may be useful to provide some geometrical interpretation (see figure 5). First of all, let us recall that whether we deal with a 2D or 3D vector field \mathbf{v} , the reconstruction problem can be handled in the 2D plane generated by the vector slopes \mathbf{p}_{ij}^+ and \mathbf{p}_{ij}^- (unless they are colinear in which case we revert to the scalar case). Then, in the case $\sigma_{ij} = 1$ (i.e when the angle $\theta_{ij} = (\mathbf{p}_{ij}^+, \mathbf{p}_{ij}^-) < \pi/2$), the set of all admissible reconstructions \mathbf{V}_{ij} is geometrically defined in this plane by the segment linking \mathbf{V}_{ij}^- and \mathbf{V}_{ij}^+ , potentially restricted to its part contained in the smallest of the two circles \mathcal{C}^- and \mathcal{C}^+ , i.e the circles of center \mathbf{V}_i and radii $\|\mathbf{V}_{ij}^{--} - \mathbf{V}_i\|$ and $\|\mathbf{V}_{ij}^{++} - \mathbf{V}_i\|$ respectively. When $\sigma_{ij} = 0$, no reconstruction is admissible and we just get $\mathbf{V}_{ij} = \mathbf{V}_i$. Now the final step is to propose VLK functions that fit in with this "vectorial second-order monotonicity area". But before that, we need to translate it in terms of the admissible interval for the values of κ_{ij} , because this is what will provide the more efficient implementation of VLK functions. This is the aim of the following section.

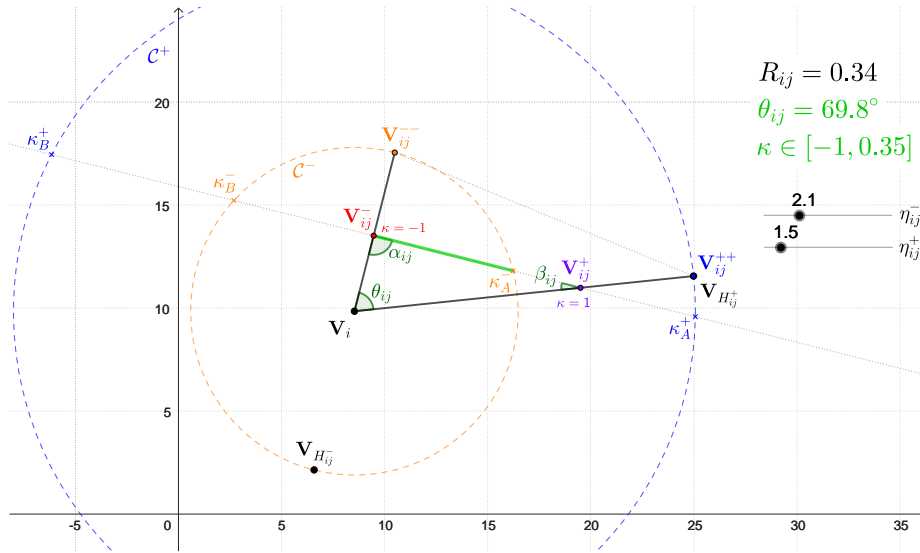


Figure 5: Representation of the "vectorial second-order monotonicity area" (figure extracted from a Geogebra applet available online [48]).

3.3. Admissible interval for κ

In this section, we will assume that $\mathbf{p}_{ij}^+ \cdot \mathbf{p}_{ij}^- > 0$, otherwise we have a local extrema and the reconstruction is just set to $\mathbf{V}_{ij} = \mathbf{V}_i$. We also assume that $\mathbf{p}_{ij}^+ \neq \mathbf{p}_{ij}^-$, otherwise the reconstruction is trivial as $\mathbf{p}_{ij} = \mathbf{p}_{ij}^+ = \mathbf{p}_{ij}^-$ and we just get $\mathbf{V}_{ij} = \mathbf{V}_i + \|\mathbf{B}_i \mathbf{M}_{ij}\| \mathbf{p}_{ij}$. Let us now associate vectors to points in the slopes plane and proceed to some geometrical calculations in this plane, mapping the values taken by κ_{ij} with the line generated by \mathbf{V}_{ij}^- and \mathbf{V}_{ij}^+ . Indeed, the values $\kappa_{ij} = -1$ and $\kappa_{ij} = 1$ are respectively associated with the points \mathbf{V}_{ij}^- and \mathbf{V}_{ij}^+ , and we seek the values of κ_{ij} corresponding to the intersection points of the line with the circles \mathcal{C}^- and \mathcal{C}^+ . Provided that $\eta_{ij}^- \geq 1$ and $\eta_{ij}^+ \geq 1^4$, two intersection points (coincident if $\eta_{ij}^- = 1$ or $\eta_{ij}^+ = 1$) do exist for both circles \mathcal{C}^- and \mathcal{C}^+ , which correspond to values of κ_{ij} that we note respectively κ_A^-, κ_B^- and κ_A^+, κ_B^+ (see figure 5).

Computing κ_A^- and κ_B^-

To obtain κ_A^- and κ_B^- , we need to solve for κ the equation

$$\|\mathbf{V}_{ij}(\kappa) - \mathbf{V}_i\| = \|\mathbf{V}_{ij}^- - \mathbf{V}_i\|, \quad (46)$$

with

$$\mathbf{V}_{ij}(\kappa) = \mathbf{V}_i + \|\mathbf{B}_i \mathbf{M}_{ij}\| \left(\frac{1-\kappa}{2} \mathbf{p}_{ij}^- + \frac{1+\kappa}{2} \mathbf{p}_{ij}^+ \right), \quad (47)$$

which can be recast as

$$\left\| \frac{1+\kappa}{2} \mathbf{p}_{ij}^+ + \frac{1-\kappa}{2} \mathbf{p}_{ij}^- \right\| = \|\eta_{ij}^- \mathbf{p}_{ij}^-\|. \quad (48)$$

Recalling that θ_{ij} is the angle between the slope vectors \mathbf{p}_{ij}^+ and \mathbf{p}_{ij}^- , and introducing R_{ij} as the ratio of their length:

$$R_{ij} = \frac{\|\mathbf{p}_{ij}^-\|}{\|\mathbf{p}_{ij}^+\|}, \quad (49)$$

then by squaring (48), and using the fact that $\|\mathbf{a}\|^2 = \mathbf{a} \cdot \mathbf{a}$ as well as $\mathbf{p}_{ij}^+ \cdot \mathbf{p}_{ij}^- = \|\mathbf{p}_{ij}^+\| \|\mathbf{p}_{ij}^-\| \cos \theta_{ij}$, we can write

$$\left(\frac{1+\kappa}{2} \right)^2 + \left(\frac{1-\kappa}{2} \right)^2 R_{ij}^2 + 2 \left(\frac{1+\kappa}{2} \right) \left(\frac{1-\kappa}{2} \right) R_{ij} \cos \theta_{ij} = (\eta_{ij}^- R_{ij})^2. \quad (50)$$

This second-order polynomial equation can be written under the form $a\kappa^2 + b\kappa + c = 0$, with:

$$\begin{cases} a &= 1 + R_{ij}^2 - 2R_{ij} \cos(\theta_{ij}) = L_{ij}^2 \\ b &= 2(1 - R_{ij}^2) \\ c &= 1 + R_{ij}^2 + 2R_{ij} \cos(\theta_{ij}) - (2\eta_{ij}^- R_{ij})^2 \end{cases}, \quad (51)$$

and

$$L_{ij} = \sqrt{1 + R_{ij}^2 - 2R_{ij} \cos \theta_{ij}} = \frac{\|\mathbf{V}_{ij}^+ - \mathbf{V}_{ij}^-\|}{\|\mathbf{V}_{ij}^+ - \mathbf{V}_i\|} = \frac{\|\mathbf{p}_{ij}^+ - \mathbf{p}_{ij}^-\|}{\|\mathbf{p}_{ij}^+\|} \geq 0, \quad (52)$$

i.e the length of the segment $[\mathbf{V}_{ij}^-, \mathbf{V}_{ij}^+]$, normalized by that of segment $[\mathbf{V}_i, \mathbf{V}_{ij}^+]$. We can then write the discriminant of (50) as

$$\Delta = 16R_{ij}^2 \left[(\eta_{ij}^- L_{ij})^2 - \sin^2 \theta_{ij} \right] = 16(R_{ij} L_{ij})^2 \left(\eta_{ij}^{-2} - \sin^2 \alpha_{ij} \right), \quad (53)$$

⁴These conditions are naturally exhibited by almost all meshes used in practice, otherwise they can still be enforced when selecting the neighbors in the multislope geometrical algorithm.

where the angle α_{ij} has been introduced thanks to the law of sines (see figure 5):

$$\frac{\|\mathbf{p}_{ij}^+ - \mathbf{p}_{ij}^-\|}{\sin \theta_{ij}} = \frac{\|\mathbf{p}_{ij}^+\|}{\sin \alpha_{ij}}. \quad (54)$$

320 We get that Δ is non-negative for any $\eta_{ij}^- \geq 1$, which leads to the following real roots of the polynomial:

$$\kappa_A^- = \frac{R_{ij}^2 - 1 + 2R_{ij}L_{ij} \left(\eta_{ij}^{-2} - \sin^2 \alpha_{ij} \right)^{1/2}}{L_{ij}^2}, \quad \kappa_B^- = \frac{R_{ij}^2 - 1 - 2R_{ij}L_{ij} \left(\eta_{ij}^{-2} - \sin^2 \alpha_{ij} \right)^{1/2}}{L_{ij}^2}. \quad (55)$$

We have $\Delta = 0$ only when $\eta_{ij}^- = 1$ and $\alpha_{ij} = \pi/2$, i.e when the line $(\mathbf{V}_{ij}^-, \mathbf{V}_{ij}^+)$ is tangent to the circle \mathcal{C}^- in $\mathbf{V}_{ij}^- = \mathbf{V}_{ij}^{--}$, implying that $\kappa_A^- = \kappa_B^- = -1$. When $\Delta > 0$, we have $\kappa_B^- < -1 < \kappa_A^-$, meaning that only κ_A^- is able to impose a restriction of the admissible interval $[-1, 1]$. Such a restriction happens when $\kappa_A^- < 1$, i.e when $\eta_{ij}^- R_{ij} < 1$.

325 *Computing κ_A^+ and κ_B^+*

To obtain κ_A^+ and κ_B^+ , we need to solve for κ the equation

$$\|\mathbf{V}_{ij}(\kappa) - \mathbf{V}_i\| = \|\mathbf{V}_{ij}^{++} - \mathbf{V}_i\| \quad (56)$$

with $\mathbf{V}_{ij}(\kappa)$ given by (47). As for κ_A^- and κ_B^- above, we can write (56) as:

$$\left(\frac{1 + \kappa}{2} \right)^2 + \left(\frac{1 - \kappa}{2} \right)^2 R_{ij}^2 + 2 \left(\frac{1 + \kappa}{2} \right) \left(\frac{1 - \kappa}{2} \right) R_{ij} \cos \theta_{ij} = (\eta_{ij}^+)^2, \quad (57)$$

which is once again a second-order polynomial equation that can be written under the form $a\kappa^2 + b\kappa + c = 0$, with:

$$\begin{cases} a &= 1 + R_{ij}^2 - 2R_{ij} \cos(\theta_{ij}) = L_{ij}^2 \\ b &= 2(1 - R_{ij}^2) \\ c &= 1 + R_{ij}^2 + 2R_{ij} \cos(\theta_{ij}) - (2\eta_{ij}^+)^2 \end{cases}. \quad (58)$$

330 We can write its discriminant as:

$$\Delta = 16 \left[(\eta_{ij}^+ L_{ij})^2 - (R_{ij} \sin \theta_{ij})^2 \right] = 16L_{ij}^2 \left(\eta_{ij}^{+2} - \sin^2 \beta_{ij} \right), \quad (59)$$

after introducing the angle β_{ij} through the law of sines. As Δ is non-negative for any $\eta_{ij}^+ \geq 1$, we obtain the following real roots of the polynomial:

$$\kappa_A^+ = \frac{R_{ij}^2 - 1 + 2L_{ij} \left(\eta_{ij}^{+2} - \sin^2 \beta_{ij} \right)^{1/2}}{L_{ij}^2}, \quad \kappa_B^+ = \frac{R_{ij}^2 - 1 - 2L_{ij} \left(\eta_{ij}^{+2} - \sin^2 \beta_{ij} \right)^{1/2}}{L_{ij}^2}. \quad (60)$$

We have $\Delta = 0$ only when $\eta_{ij}^+ = 1$ and $\beta_{ij} = \pi/2$, i.e when the line $(\mathbf{V}_{ij}^-, \mathbf{V}_{ij}^+)$ is tangent to the circle \mathcal{C}^+ in $\mathbf{V}_{ij}^+ = \mathbf{V}_{ij}^{++}$, implying that $\kappa_A^+ = \kappa_B^+ = 1$. When $\Delta > 0$, we have $\kappa_B^+ < 1 < \kappa_A^+$, meaning that only κ_B^+ is able to impose a restriction of the admissible interval $[-1, 1]$. Such a restriction only happens when $\kappa_B^+ > -1$, i.e when $R_{ij} > \eta_{ij}^+$.

Summary

To summarize, any VLK function $\kappa_{ij} = \kappa(\mathbf{p}_{ij}^+, \mathbf{p}_{ij}^-, \eta_{ij}^+, \eta_{ij}^-)$ has to satisfy:

$$\boxed{\max(-1, \kappa_B^+(R_{ij}, \theta_{ij}, \eta_{ij}^+)) \leq \kappa_{ij} \leq \min(1, \kappa_A^-(R_{ij}, \theta_{ij}, \eta_{ij}^-))}. \quad (61)$$

In other words, the admissible interval I_κ is defined as:

$$I_\kappa = \left[\max(-1, \kappa_B^+(R_{ij}, \theta_{ij}, \eta_{ij}^+)), \min(1, \kappa_A^-(R_{ij}, \theta_{ij}, \eta_{ij}^-)) \right], \quad (62)$$

340 with

$$\kappa_A^- = \frac{R_{ij}^2 - 1 + 2R_{ij} ((\eta_{ij}^- L_{ij})^2 - \sin^2 \theta_{ij})^{1/2}}{L_{ij}^2}, \quad \kappa_B^+ = \frac{R_{ij}^2 - 1 - 2((\eta_{ij}^+ L_{ij})^2 - \sin^2 \theta_{ij})^{1/2}}{L_{ij}^2}. \quad (63)$$

Note that when slopes are colinear with $\theta_{ij} = 0$, the bounding functions κ_A^- and κ_B^+ reduce to the scalar functions κ^- and κ^+ defined by (25) (see details in Appendix C.4). This means that the vectorial framework described above does reduce to the classical multislope scalar framework when slopes are colinear, which fulfills one of the initial objectives. Let us also stress that the method described above can be implemented
 345 very easily, and with a very limited additional cost versus a componentwise approach. Indeed, we only deal with the slopes vectors in the usual compact stencil, without needing to compute a convex hull or any similar heavy geometric object.

3.4. Definition of VLK functions

We introduce in this section some VLK functions derived from classical scalar LK functions, namely
 350 Monotonized Central, Minmod and Superbee. These VLK functions are illustrated on the example given in Figure 6, and also plotted in figures 7 and 8 with R_{ij} as the x -variable, for different values of θ_{ij} , η_{ij}^+ and η_{ij}^- . It is also worth mentioning that it is possible to express VLK functions in a "limiter function" formalism, which provides additional understanding regarding the connection with the scalar case (see Appendix C).

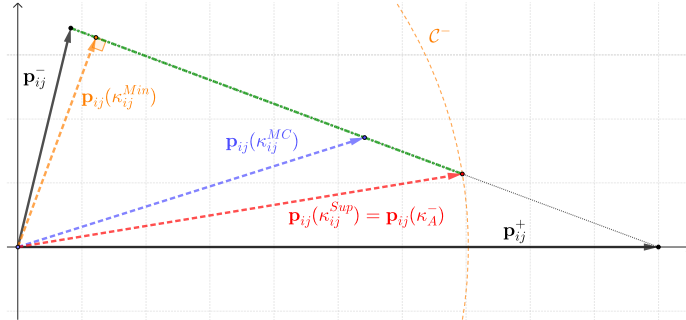


Figure 6: Representation of the Monotonized Central ($\kappa_0 = 0$), Minmod and Superbee VLK functions in terms of the effective slope $\mathbf{p}_{ij}(\kappa_{ij})$.

3.4.1. Monotonized Central VLK

355 The Monotonized Central VLK function is defined such that $\kappa_{ij} = \kappa_0$ as long as that there is no local extremum ($\sigma_{ij} = 1$) and κ_0 belongs to the admissible interval I_κ defined by relation (62). Otherwise, we retain the bound of I_κ which is the closest to κ_0 . When $\sigma_{ij} = 1$, we can therefore write:

$$\kappa_{ij}^{MC}(R_{ij}, \theta_{ij}, \eta_{ij}^+, \eta_{ij}^-) = \max(\kappa_B^+, \min(\kappa_0, \kappa_A^-)) = \begin{cases} \kappa_0 & \text{if } \kappa_0 \in I_\kappa \\ \kappa_B^+ & \text{if } \kappa_0 < \kappa_B^+ \\ \kappa_A^- & \text{if } \kappa_0 > \kappa_A^- \end{cases}. \quad (64)$$

If $\sigma_{ij} = 0$, no reconstruction is admissible and we just take $\mathbf{V}_{ij} = \mathbf{V}_i$. A Monotonized Central function is usually based on the Fromm scheme such that $\kappa_0 = 0$, but it is possible to use any value $\kappa_0 \in [-1, 1]$. For
 360 example, a Koren VLK function could be built using $\kappa_0 = 1/3$.

3.4.2. Minmod VLK

By extension of the scalar Minmod limiter, we define the Minmod VLK function as the one which brings about the smallest effective slope $\|\mathbf{p}_{ij}\|$, provided that κ_{ij} belongs to the admissible interval (62). In the scalar case, the smallest effective slope is always either the forward slope p_{ij}^+ , or the backward slope p_{ij}^- , but this is no longer true in the vectorial case. In the vectorial case indeed, the smallest effective slope is defined by the altitude of triangle $(\mathbf{V}_{ij}^-, \mathbf{V}_i, \mathbf{V}_{ij}^+)$ from \mathbf{V}_i , under the condition that it intersects the segment $[\mathbf{V}_{ij}^-, \mathbf{V}_{ij}^+]$, i.e if there is no obtuse angle in \mathbf{V}_{ij}^- or \mathbf{V}_{ij}^+ . Otherwise the effective slope is equal to the backward slope (respectively to the forward slope) if the obtuse angle is in \mathbf{V}_{ij}^- (respectively in \mathbf{V}_{ij}^+). For $\sigma_{ij} = 1$, this Minmod VLK function then reads:

$$\kappa_{ij}^{Min}(R_{ij}, \theta_{ij}) = \max(-1, \min(\kappa_{ij}^H, 1)), \quad (65)$$

with κ_{ij}^H the value of κ corresponding to the intersection point of the altitude from \mathbf{V}_i with the line $(\mathbf{V}_{ij}^-, \mathbf{V}_{ij}^+)$, which is given by:

$$\kappa_{ij}^H = 1 - 2 \frac{1 - R_{ij} \cos \theta_{ij}}{L_{ij}^2} = 1 - \frac{2}{1 + \frac{R_{ij} - \cos \theta_{ij}}{R_{ij}^{-1} - \cos \theta_{ij}}}. \quad (66)$$

Note that like in the scalar case, the geometrical parameters η_{ij}^- and η_{ij}^+ are not involved in the definition of the Minmod VLK function. Since we consider the smallest slope, the monotonicity constraint in which the geometrical parameters η_{ij}^+ and η_{ij}^- appear is not relevant anymore.

3.4.3. Superbee VLK

Equivalently to its scalar definition, we can define the Superbee VLK function as the one giving the highest effective slope $\|\mathbf{p}_{ij}\|$, provided that κ_{ij} belongs to the admissible interval (62). As we have the following inequalities:

$$\kappa_A^- < 1 \text{ if } R_{ij} < \frac{1}{\eta_{ij}^-} < 1, \quad \kappa_B^+ > -1 \text{ if } R_{ij} > \eta_{ij}^+ > 1, \quad (67)$$

then we have to distinguish four cases to write this limiting function, which reads:

$$\kappa_{ij}^{Sup}(R_{ij}, \theta_{ij}, \eta_{ij}^+, \eta_{ij}^-) = \begin{cases} \kappa_A^- & \text{if } 0 \leq R_{ij} < 1/\eta_{ij}^- \\ 1 & \text{if } 1/\eta_{ij}^- \leq R_{ij} < 1 \\ -1 & \text{if } 1 < R_{ij} \leq \eta_{ij}^+ \\ \kappa_B^+ & \text{if } R_{ij} > \eta_{ij}^+ \end{cases}. \quad (68)$$

However the Superbee VLK function is not entirely defined as this, because we still have to define a value κ_{ij}^{Sup} for $R_{ij} = 1$, knowing that both $\kappa_{ij}^{Sup} = 1$ and $\kappa_{ij}^{Sup} = -1$ are possible choices. In the scalar case, all κ -schemes are equivalent when $r_{ij} = 1$, but this is no more true in the vectorial case when $R_{ij} = 1$ (except of course when $\theta_{ij} = 0$, i.e when we recover the scalar case). The ambiguity could be resolved by making an arbitrary choice between both possibilities. Nevertheless, this limited reconstruction does not seem to be a very good idea as it is likely to result in bad convergence properties for the overall scheme, due to the Superbee VLK function switching between two very different solutions. The vectorial extension of the Superbee limiter is thus possible, but does not seem really judicious.

4. Numerical results

In this section, several test-cases are provided to assess the new vectorial reconstruction method. Different methods are tested for each case, which are referred to with acronyms throughout the section. Hence, **CW** stands for a Component-Wise reconstruction, while **VLKS** stands for the new Vectorial Limited Kappa

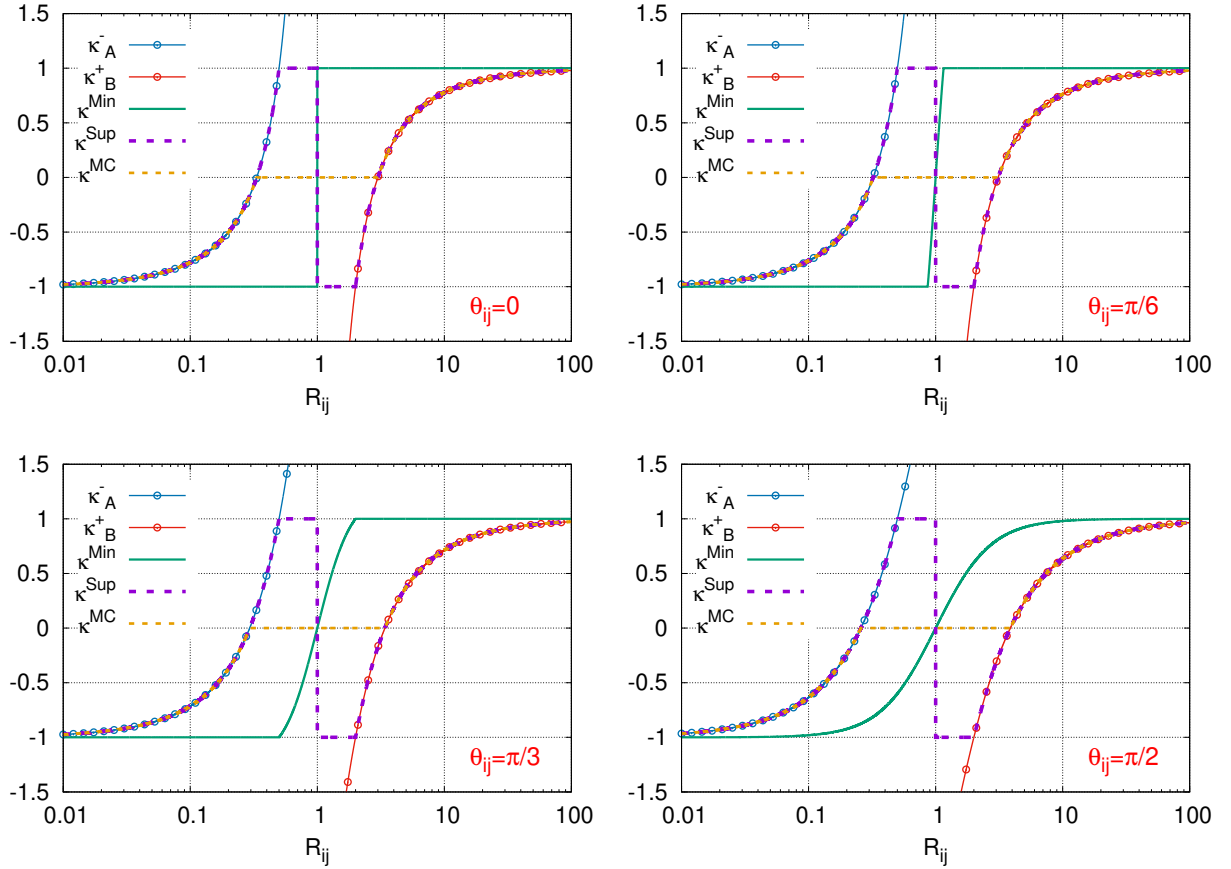


Figure 7: Plot of $\kappa_{ij}(R_{ij}, \theta_{ij}, \eta_{ij}^+, \eta_{ij}^-)$ for the Monotonized Central ($\kappa_0 = 0$), Minmod and Superbee VLK functions, with $\eta_{ij}^- = \eta_{ij}^+ = 2$ (cartesian mesh) and several values of θ_{ij} .

Scheme. Regarding the limiting function, **MC**, **Sup** and **Min** respectively stand for the Monotonized Central (with $\kappa_0 = 0$), Superbee and Minmod limiting functions (either in scalar or in vector forms). Furthermore we will denote by **NL** a non-limited scheme using $\kappa_0 = 0$ as parameter, which basically corresponds to the Fromm scheme, and by **O1** a scheme with a first-order reconstruction. Unless stated otherwise, the time discretization is performed with the low-storage fourth-order Strong Stability Preserving Runge-Kutta method described in [49] and usually noted as SSPRK(10,4), with a Courant number CFL = 2. For the physical benchmarks of sections 4.2 to 4.5, the computations are performed with the CFD platform CEDRE [24], which solves the compressible Euler or Navier-Stokes equations. The HLLC approximate Riemann solver is then used together with the multislope MUSCL method, with the scalar variables like pressure, temperature or density reconstructed with a classical scalar limiter (MC or van Leer).

4.1. Rotation test cases

In order to test the accuracy, robustness and performance of the vectorial reconstruction methods, let us consider the rotation of several 2D or 3D vector fields \mathbf{v} by a velocity field $\mathbf{\lambda}$, as described by the vectorial advection equation (31). For each case, the eight vectorial reconstruction methods listed in the introduction of the section are compared. Each 2D simulation is run for a duration $t_f = 10$ ms corresponding to ten revolutions of the vector field, while the 3D simulations are run for a duration $t_f = 1$ ms corresponding to one revolution only. In order to evaluate the spatial accuracy, we consider triangular (in 2D) or tetrahedral (in 3D) unstructured meshes of increasing refinement. Each refinement is characterized through the size h

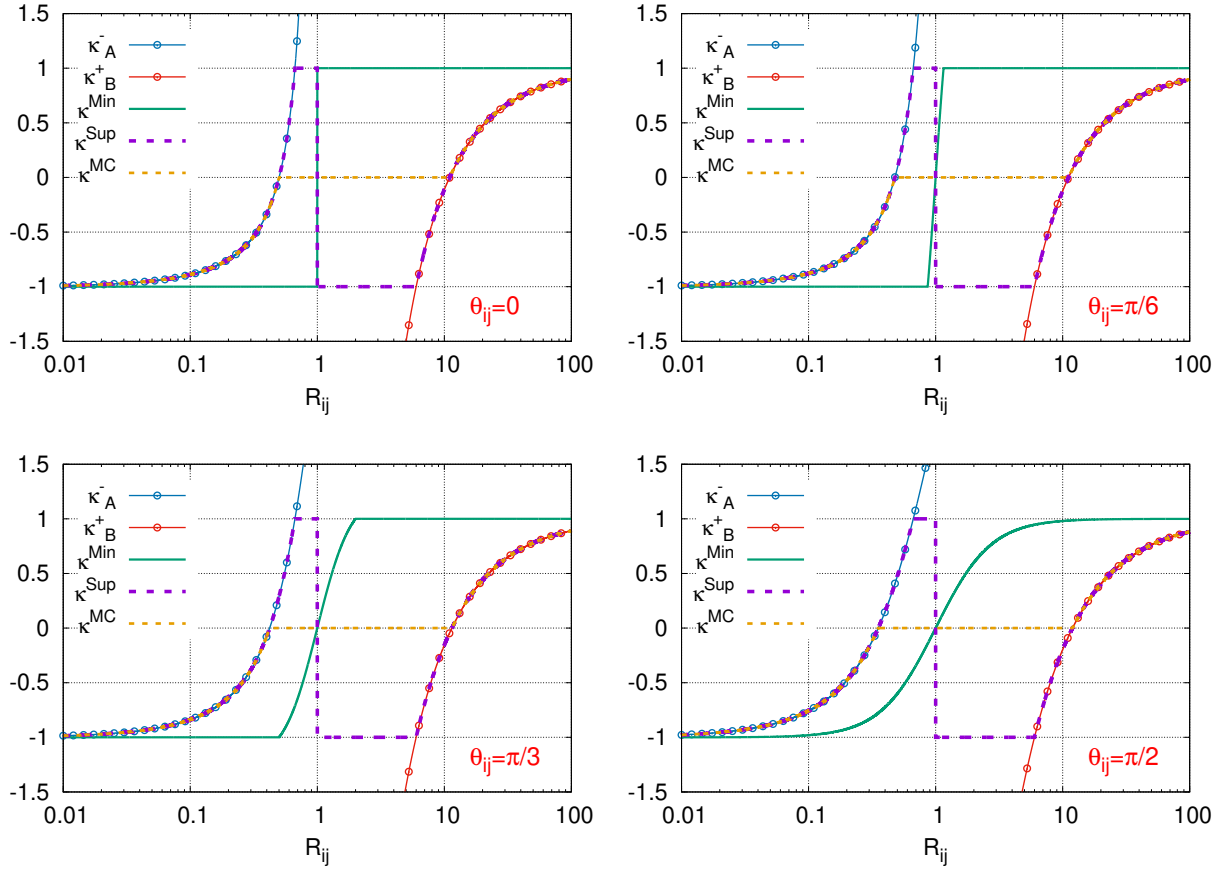


Figure 8: Plot of $\kappa_{ij}(R_{ij}, \theta_{ij}, \eta_{ij}^+, \eta_{ij}^-)$ for the Monotonized Central ($\kappa_0 = 0$), Minmod and Superbee VLK functions, with $\eta_{ij}^- = 1.5$ et $\eta_{ij}^+ = 6$ (unstructured mesh) and several values of θ_{ij} .

410 defined by:

$$h \approx \left(\frac{|\Omega|}{\mathcal{N}} \right)^{1/d}, \quad (69)$$

with \mathcal{N} the number of cells in the mesh, d the dimension of the space and $|\Omega|$ the measure of the domain (area or volume). Six different mesh refinements are considered for the 2D cases, namely $h = 5, 10, 15, 20, 25, 30$ mm, while for the 3D case we only consider four different meshes with $h = 10, 20, 40, 80$ mm. To assess the spatial accuracy of each approach, we define the error in L^1 norm as follows:

$$\epsilon_1 = \sum_{K_i} |K_i| \| \mathbf{V}_i(t_f) - \mathbf{V}_i(t_0) \|_2, \quad (70)$$

415 while the error in L^∞ norm is defined as

$$\epsilon_\infty = \max_{K_i} \| \mathbf{V}_i(t_f) - \mathbf{V}_i(t_0) \|_2. \quad (71)$$

In these definitions, $\mathbf{V}_i(t_f)$ is the discrete solution at the center of each cell K_i at the final time, and $\mathbf{V}_i(t_0)$ is the initial solution and also the expected exact solution. The L^1 norm is interesting for both discontinuous and smooth cases, as it stands for the global diffusive error of the scheme, while the L^∞ norm is only relevant for smooth cases since it represents the loss of amplitude of the convected function. In the

420 asymptotic limit $h \rightarrow 0$, the error satisfies $\epsilon_n = C_n h^{\alpha_n}$ (with C_n a constant depending on the norm L^n), therefore the effective order of the scheme α_n can be approximated by computing the linear regression of $\log(\epsilon_n) = \alpha_n \log h + \log C_n$.

4.1.1. Smooth annular vector field (2D)

425 For this test-case and all the 2D cases, we consider a circular computational domain Ω with a radius $R_0 = 1$ and a divergence-free velocity field $\lambda(x, y) = 10^3 \times 2\pi(-y \ x)^t$. Each face at the boundary has a normal vector orthogonal to the velocity vector, hence their scalar product and the numerical flux vanish. Let us consider a smooth annular vector field $\mathbf{v}_0(x, y)$ whose direction is radial and with a norm given by:

$$\|\mathbf{v}_0\| = V_0 \times \begin{cases} 0 & \text{if } 0 < R \leq 0.1 \\ \sin^2\left(\frac{5\pi}{2}R - \frac{\pi}{4}\right) & \text{if } 0.1 < R \leq 0.3 \\ 1 & \text{if } 0.3 < R \leq 0.6 \\ \sin^2\left(-\frac{5\pi}{2}R + 2\pi\right) & \text{if } 0.6 < R \leq 0.8 \\ 0 & \text{if } 0.8 < R \leq 1 \end{cases}, \quad (72)$$

with $R = \sqrt{x^2 + y^2}$ and $V_0 = 5000$. Figure 9a shows the time evolution of $\|\mathbf{V}\|_\infty = \max_{K_i \in \Omega} \|\mathbf{V}_i\|$ obtained with all schemes on the coarsest mesh, figure 10 displays the error in both L^1 and L^∞ norms versus the mesh size for the different methods, while figure 11 shows the contour plot of the vector norm at the final time t_f for the mesh $h = 30$ mm obtained with each method (except for the overly diffusive O1 and the unstable VLKS-Sup methods that we have skipped). We see that the accuracy of VLKS and CW methods is very comparable when using MC and Min limiters, and that both MC schemes show an accuracy similar to that of NL. This is expected on such a smooth case where limitation is not really required, since the NL scheme is based on the same second-order linear scheme as MC (with $\kappa_0 = 0$). It also appears that CW-Sup exhibits the lowest accuracy among the stable second-order schemes, which is an expected result due to its well-known squaring effect on smooth solutions, while VLKS-Sup is clearly unstable (the error increases when the mesh is refined). Moreover, figure 12 shows the same final solutions as figure 11, but with a $\pi/4$ rotation of the initial vector field. This mimics a rotation of the reference frame, to which a frame-independent vectorial method should be insensitive due to the radial symmetry of the vector field. What we see is that all CW methods break the radial symmetry of the solution, which also means that they turn out to be frame dependent. Indeed, four spots of increased value of the norm are created, whose location at the final time depends on the orientation of the reference frame. On the other hand, symmetry and frame-independency are verified by the VLKS schemes. Finally, normalized CPU costs are provided in table 2. Note that these costs could be compared only between the different methods on a given mesh. The comparison between different meshes is not relevant as each set of simulations for a given mesh may have run on a different machine. It appears that VLKS methods are slightly more expensive than their CW counterparts, with an increase of the CPU cost between 10 and 15 %. This is very reasonable for a real vectorial reconstruction method, especially when we consider that on these simple rotation cases, the cost of the reconstruction procedure represents most of the CPU time consumption. This should be much less significant when applied to a real system of PDE with physical models.

4.1.2. Sinusoidal vector field (2D)

We now consider a sinusoidal vector field that mimics a vortical flow which reads:

$$\mathbf{v}_0(x, y) = V_0 \begin{pmatrix} \sin(2\pi x) + \sin(2\pi y) \\ \sin(2\pi x) - \sin(2\pi y) \end{pmatrix}, \quad (73)$$

455 with $V_0 = 5000$. Figure 9b shows the time evolution of $\|\mathbf{V}\|_\infty$ obtained with all schemes on the coarsest mesh, which illustrates a behavior previously exposed regarding the CW approach and the maximum principle. As explained in section 3.1, the CW approach does not imply a maximum principle on the vector magnitude but only a maximum principle on each component individually. This means that the magnitude can increase but only to the point that it reaches the maximum allowable value characterized by the corner of the "bounding box" represented in a schematic way in figure 4. Considering the definition (73) of the initial vector field,

Method	$h = 0.005$	$h = 0.01$	$h = 0.015$	$h = 0.02$	$h = 0.025$	$h = 0.03$
O1	14.17	10.08	8.50	6.61	5.50	4.84
CW-Min	22.88	16.62	14.54	11.76	9.42	8.29
CW-MC	20.46	16.40	14.66	11.72	9.50	8.27
CW-Sup	20.50	16.82	14.72	11.65	9.50	8.27
VLKS-Min	21.57	17.70	16.05	12.97	10.83	9.60
VLKS-MC	22.55	17.66	15.93	13.03	10.78	9.53
VLKS-Sup	22.20	18.31	16.66	13.67	11.36	10.05
NL	20.98	16.41	14.65	11.65	9.48	8.29

Table 2: CPU cost ($\mu\text{s}/\text{iteration}/\text{mesh cell}$) for the case of the smooth vector field (annular).

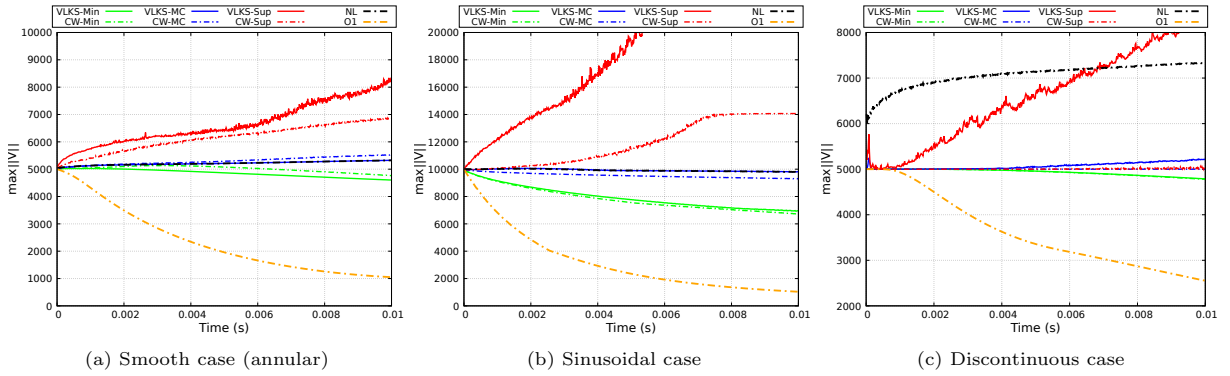


Figure 9: Time evolution of $\|\mathbf{V}\|_\infty$ on the mesh $h = 30$ mm for the 2D cases.

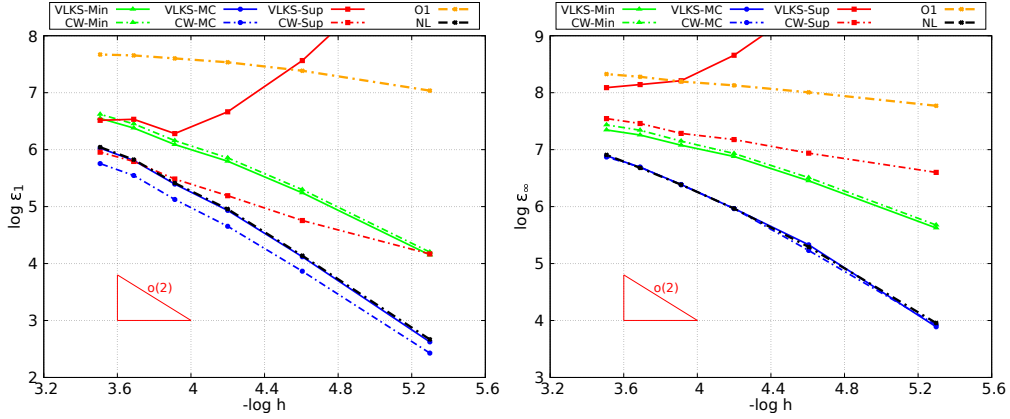


Figure 10: Errors in L^1 and L^∞ norms for the smooth case (annular). Data for the last points of the VLKS-Sup method is out of scale as the computation is unstable (the error increases as the mesh is refined).

460 this maximum value can be computed as $V_{max} = \sqrt{v_{x,max}^2 + v_{y,max}^2} \approx 14,142$, which is almost exactly the
maximum value reached here with the CW-Sup scheme. Figure 13 displays the error in both L^1 and L^∞
norms versus the mesh size for the different methods, while figure 14 shows the contour plot of the vector
norm at the final time t_f for the mesh $h = 30$ mm obtained with each method (except again for O1 and
VLKS-Sup). The behavior of the different schemes regarding accuracy is similar on this case to what was
465 observed on the smooth annular case. The normalized CPU costs are also similar to those provided in table
2 for the smooth annular vector field and are thus not provided here.

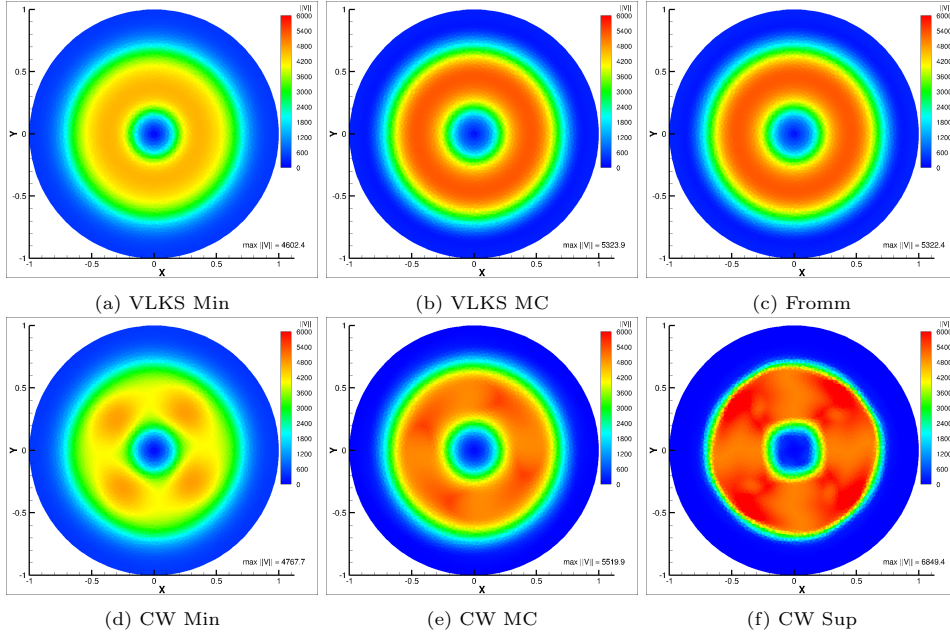


Figure 11: Comparison of the final vector fields for the smooth case (annular). Mesh $h = 30$ mm.

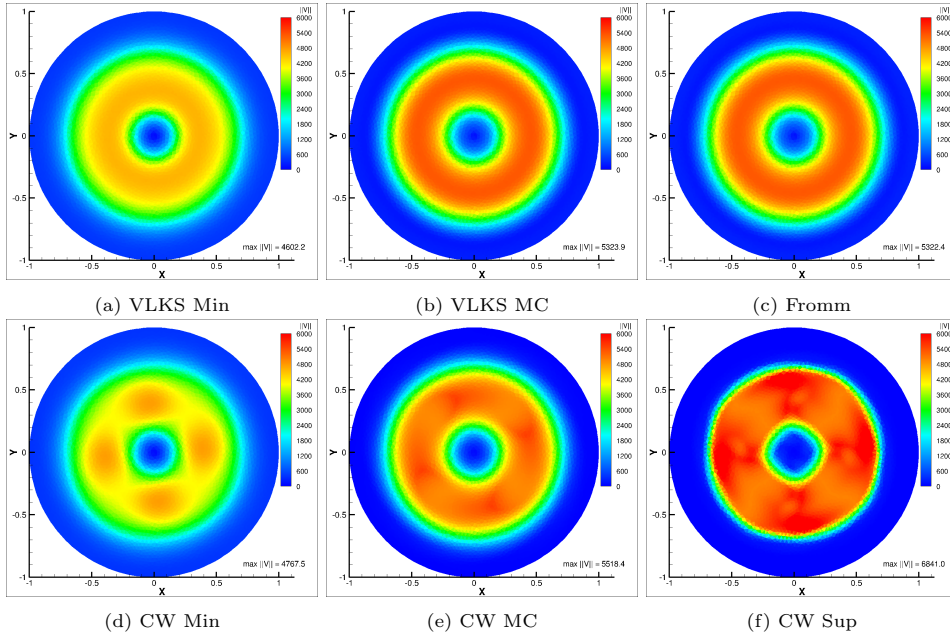


Figure 12: Comparison of the final vector fields for the **rotated** smooth case (annular). Mesh $h = 30$ mm.

4.1.3. Sinusoidal vector field (3D)

For the 3D test-case, we consider a cylindrical domain with the divergence-free velocity field

$$\lambda(x, y, z) = 10^3 \begin{pmatrix} -2\pi y \\ 2\pi x \\ 2 \end{pmatrix}. \quad (74)$$

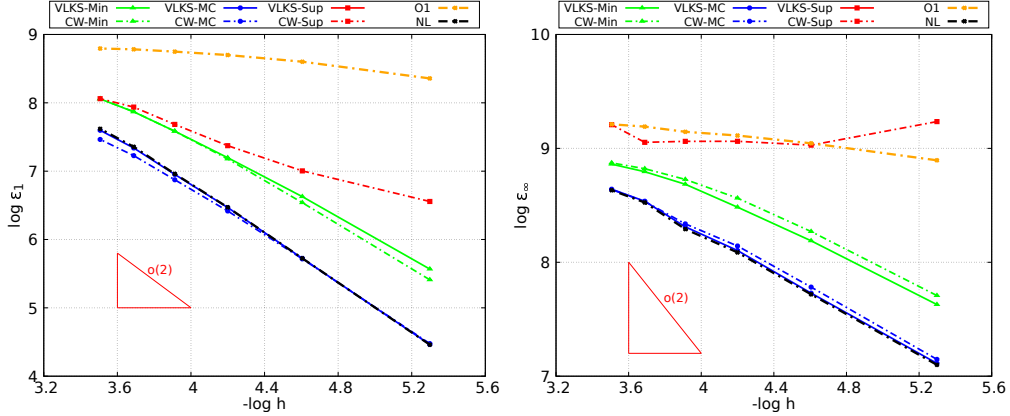


Figure 13: Errors in L^1 and L^∞ norms for the sinusoidal case. Data for the VLKS-Sup method is out of scale as the computation is unstable (the error increases as the mesh is refined).

470 The circular domain of the 2D cases is here extruded in the z direction, and periodic boundaries are set at the top and bottom sides of the cylinder. Similarly, the velocity field is an extension of the one previously used for 2D cases, with a constant z -component such that the streamlines follow a spiral shape. The following 3D vector field is considered:

$$\mathbf{v}_0(x, y, z) = V_0 \begin{pmatrix} \sin \bar{x} + \sin \bar{y} \\ \sin \bar{x} - \sin \bar{y} \\ R \sin \bar{z} \end{pmatrix}, \quad (75)$$

475 with $\bar{x} = 2\pi x/L_x$, $\bar{y} = 2\pi y/L_y$, $\bar{z} = 2\pi z/L_z$, $R = \sqrt{x^2 + y^2}$, $V_0 = 5000$ and the wavelengths set to $L_x = L_y = 1$ and $L_z = 2$. We only compute one revolution of the vector field (vs. ten revolutions in the 2D case) due to the high cost of the 3D meshes, and only provide the error plots for the different methods in figure 15. Regarding both accuracy and CPU costs, the results for this case are again similar to those of the smooth annular vector field, demonstrating that VLKS behaves in a similar way on 3D meshes.

4.1.4. Discontinuous vector field (2D)

480 For this discontinuous case, we split the circular domain in four sectors in which the initial vector field $\mathbf{v}_0(x, y)$ is set constant with only one component nonvanishing and equal to $V_0 = 5000$. This discontinuous vector field reads:

$$\mathbf{v}_0(x, y) = V_0 \begin{cases} \begin{pmatrix} 1 & 0 \end{pmatrix}^t & \text{if } y < 0 \text{ and } x \geq 0, \\ \begin{pmatrix} -1 & 0 \end{pmatrix}^t & \text{if } y < 0 \text{ and } x < 0, \\ \begin{pmatrix} 0 & 1 \end{pmatrix}^t & \text{if } y \geq 0 \text{ and } x \geq 0, \\ \begin{pmatrix} 0 & -1 \end{pmatrix}^t & \text{if } y \geq 0 \text{ and } x < 0. \end{cases} \quad (76)$$

485 Figure 9c shows the time evolution of $\|\mathbf{V}\|_\infty$ obtained with all schemes on the coarsest mesh, figure 16 displays the error in L^1 norm versus the mesh size for the different methods, while figure 17 shows the contour plot of the vector norm at the final time t_f for the mesh $h = 10$ mm, obtained with each method. CW-Sup is here the most accurate of all methods, which is not surprising. As the CW approach deals with each vector component as a scalar, we naturally get the well-established good behavior of the classical Superbee when it comes to transport scalar discontinuities. On the other hand, VLKS-Sup is unstable once again and therefore not even suitable for the transport of discontinuous solutions, whereas VLKS and CW show similar results when equipped with both MC and Min limiting functions, thereby preserving the scheme stability.

4.1.5. Conclusions from the rotation cases

490 Let us now sum up the main conclusions from the rotation cases described above. Whether it be with the CW or the VLKS approach, we have the expected result that the Monotonized Central versions are the most

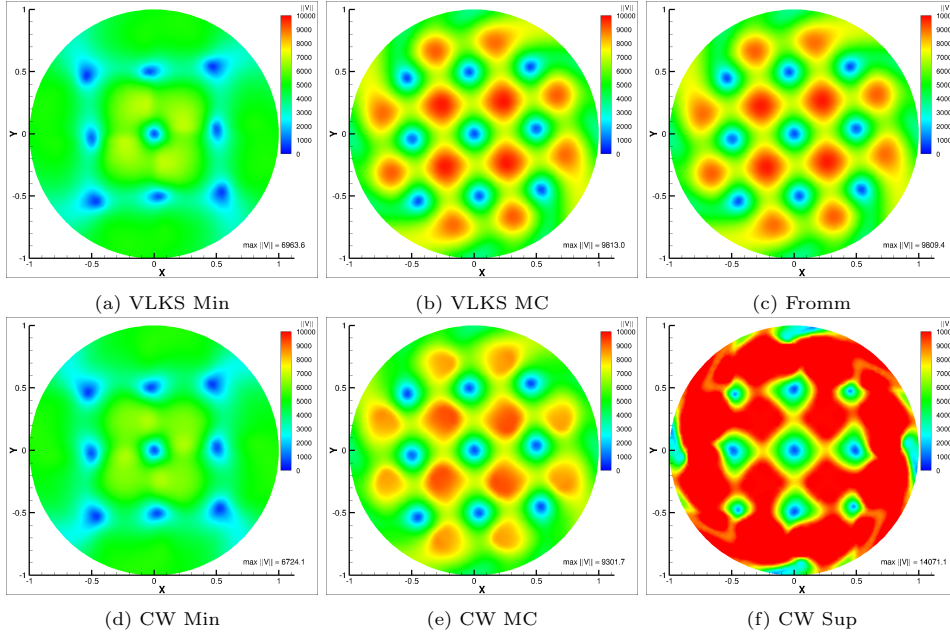


Figure 14: Comparison of the final vector fields for the sinusoidal case. Mesh $h = 30$ mm.

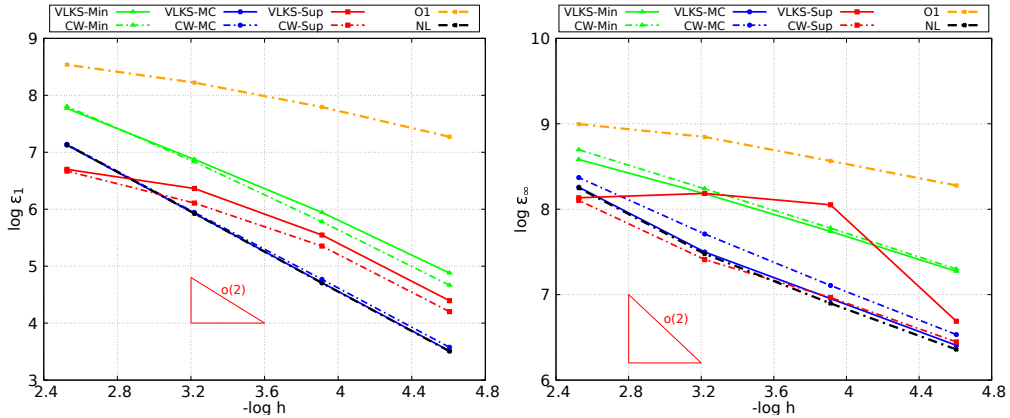


Figure 15: Errors in L^1 and L^∞ norms for the sinusoidal case (3D).

accurate, while Minmod are the most dissipative and Superbee is only good at capturing discontinuities. Actually, CW-Sup is the most accurate when it only comes to capture discontinuities, while VLKS-Sup is mostly unstable, even for smooth cases. It seems that selecting always the maximum vector slope leads to a very poor stability behavior of the VLKS-Sup scheme, despite the limiting procedure described in section 3.4.3. As expected, the second-order non limited Fromm scheme shows a good accuracy for smooth solutions for which limiting is not required. However it triggers more or less severe overshoots when discontinuities or stiff variations are involved. On smooth solutions, the order of accuracy of the VLKS schemes (apart from VLKS-Sup) is very comparable with their CW counterparts (sometimes better, see e.g the L^∞ error on the sinusoidal and 3D case for VLKS-MC vs. CW-MC). This means a lesser diffusion of the amplitude of the solutions, which can have an importance for the simulations involving physics (see e.g. the CFD cases of sections 4.3 and 4.4). Besides, the overall quality of the solution seems better. Indeed, the CW approach tends to break the symmetry of the solution as can be seen for instance in figure 11, and in top of that in a way that is frame-dependent (compare figures 11 and 12 which show the same computation on the same

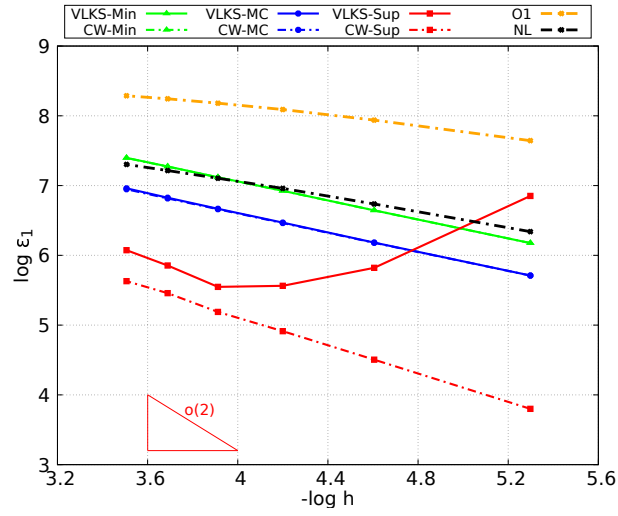


Figure 16: Error in L^1 norm for the discontinuous case.

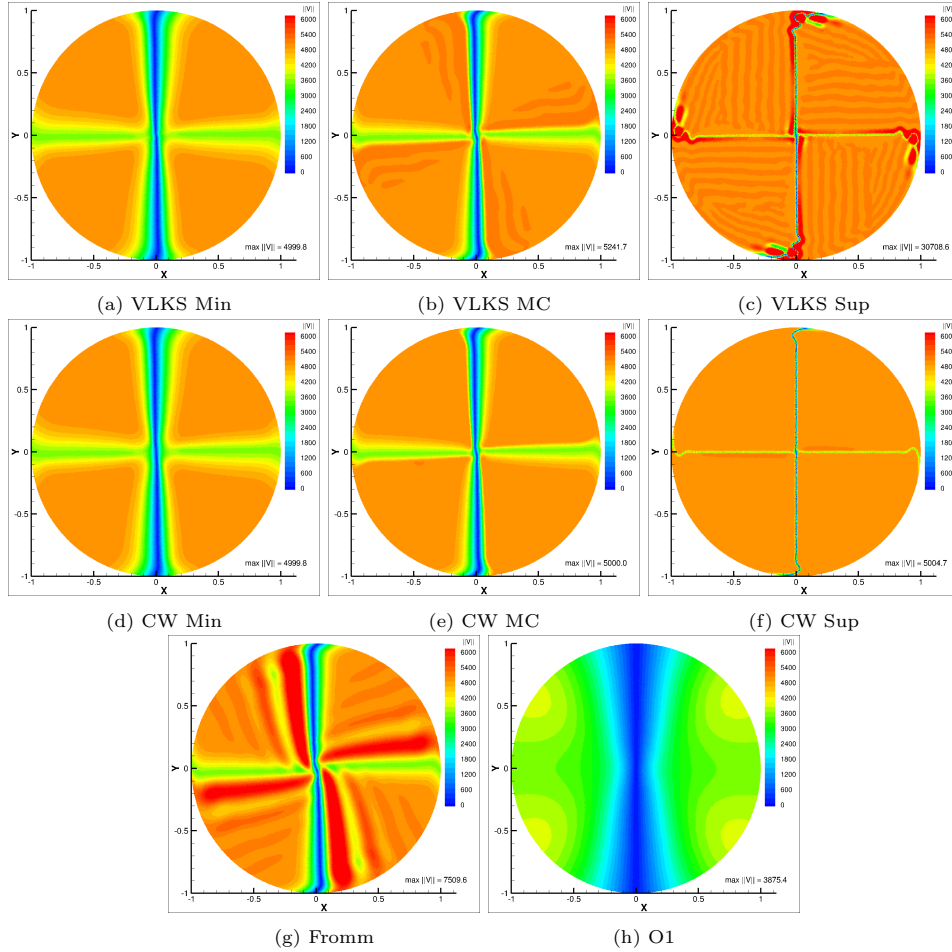


Figure 17: Comparison of the final vector fields for the discontinuous case. Mesh $h = 10$ mm.

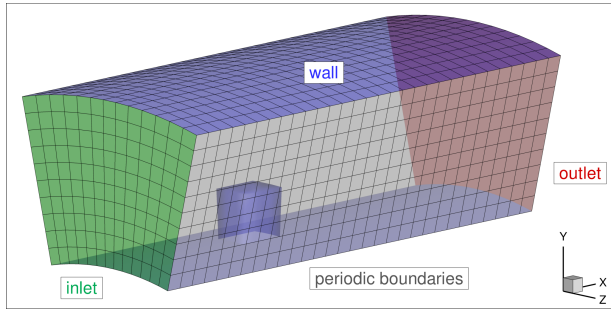


Figure 18: View of the geometry, mesh and boundary conditions for the turbomachinery test-case (initial position). The second position is obtained by applying a 90° rotation around the axis defined by the origin and the vector $(1, 1, 1)$.

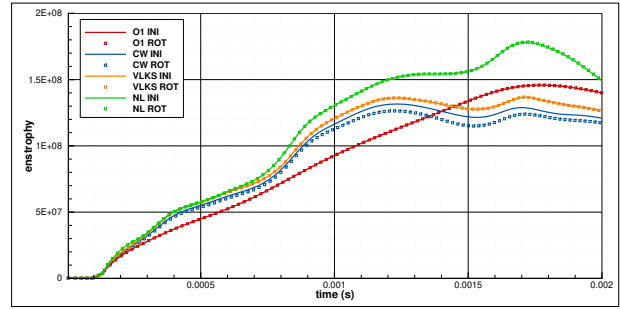


Figure 19: Volume integral of the enstrophy over time for the four tested methods on each geometry (initial and rotated).

mesh, but with a rotation of the reference frame). The results obtained with the VLKS-MC scheme are very close to that of the Fromm scheme for smooth solutions, while they are better for discontinuities. We still notice small overshoots of the vector magnitude (the method exhibits no maximum principle on the vector magnitude) but they remain very limited and are not amplified. Anyhow they are not higher than the overshoots on the magnitude also exhibited by CW methods.

To conclude, these rotation test cases show that the new VLKS approach exhibits a good second-order accuracy, similar or sometimes slightly better than CW, especially regarding the preservation of the amplitude of solutions. In the meantime, it avoids some defects of CW, such as the frame-dependency and the tendency to break the radial symmetry, with a very limited extra CPU cost. Especially, the VLKS-MC method seems the best VLKS option, so it will be primarily used for the numerical tests of the next sections dedicated to physical cases.

4.2. Turbomachinery test-case with rotationally periodic boundary conditions

We consider a test-case representative of turbomachinery engineering applications in CFD, whose objective is twofold. First, we want to illustrate the non-frame-invariant behavior of the componentwise vectorial approach when using non-linear second-order limiters. And secondly, we want to illustrate that when using rotationally periodic boundary conditions, which is classical in such applications, this non-frame-invariant feature can turn into a conservation issue. The vectorial approach proposed in this paper is shown to be frame-invariant and therefore naturally avoids the conservation issue.

The case we consider is very simplified in order to focus on the point we want to make, so it does not represent any real engineering application. The 3D geometry is represented in figure 18 with the boundary conditions and the associated structured mesh, made up with approximately 4,000 cells and 12,000 faces. It consists of a cavity rotating with an angular velocity $\omega = 50$ rad/s around the x-axis, initially filled with air at rest under atmospheric conditions. The air injected through the inlet with a velocity of 300 m/s (normal to the boundary) is then driven into a rotational motion due to the rotating reference frame, so that it crosses the periodic boundaries before exhausting through the outlet. The rotational periodicity is defined by the x-axis and a 28° angle, while the other boundary conditions are adiabatic walls. Time integration is performed with a RK2 scheme and a time step driven by a maximum CFL value of 0.4, for a total computation time of 2 ms.

In order to assess the frame invariance of these different methods, we will also consider an alternative geometry with a different orientation in space. It is obtained by applying to the first geometry represented in figure 18 a 90° rotation around the axis passing through the origin and whose direction is given by the vector $(1, 1, 1)$. In what follows, INI will refer to the initial geometry represented in figure 18, while ROT will refer to the rotated geometry. In order to provide a quantitative assessment of the frame invariance, any integral quantity based on the velocity vector field can be used. We choose the volume integral of the

enstrophy, defined as:

$$\mathcal{E}(t) = \frac{1}{2} \int_{\Omega} \rho(\mathbf{x}, t) \|\nabla \times \mathbf{V}(\mathbf{x}, t)\|^2 d\mathbf{x}, \quad (77)$$

where $\rho(\mathbf{x}, t)$ and $\mathbf{V}(\mathbf{x}, t)$ are the fluid density and velocity vector at a given point \mathbf{x} at time t , and with $\nabla \times$ the rotational operator. For each vectorial reconstruction method, we plot in figure 19 the enstrophy evolution over time obtained on both the initial and rotated geometries. It is clear that for the componentwise second-order method, the enstrophy plots are gradually diverging. This is a direct consequence of the method being not frame-invariant due to the non-linearity of the scalar limiter used for each component. On the other hand, all the other methods are indeed frame-invariant.

Now we want to highlight the fact that the non-invariance issue may turn into a conservation issue when dealing with rotationally periodic boundary conditions. Indeed, in such cases the fluxes through the periodic boundaries are computed twice, once for each boundary. And for the simulation to be conservative, we need that the numerical flux computed through one boundary be the exact opposite of the flux computed through the other boundary. To achieve this, an exchange of information is required (potentially through MPI communications for instance) so that each boundary knows the "left" and "right" velocity vectors to be used in the Riemann solver. More specifically, the usual procedure for that in a cell-centered finite volume code is as follows: exchange the physical quantities (including the velocity vectors \mathbf{V}_i and \mathbf{V}_j) at the cell centers adjacent to the boundary faces, apply the rotation to vectors to account for the periodicity, perform the MUSCL interpolations of the variables (including the velocity vectors \mathbf{V}_{ij} and \mathbf{V}_{ji}), and finally compute the numerical flux. If the MUSCL interpolation of vectors is not frame-independent, then in the general case we won't have the equality of the scalar product $\mathbf{V}_{ij} \cdot \mathbf{n}_{ij}$, which directly implies that we cannot have the conservation of the flux. To illustrate this issue, figure 20 shows the temporal evolution of the energy flux integrated over the surface area of both periodic boundaries, as well as their sum, for all the considered methods on the initial geometry. Once again, only the second-order componentwise method is found to be non frame-invariant and therefore not conservative through the periodic boundaries. The conservation error fluctuates throughout the computation but can rise up to the same order of magnitude as the value of the flux itself. For all the other methods, the conservation error is almost zero (of the order of machine epsilon).

To conclude, let us mention that it remains sometimes possible to apply a patch to correct the componentwise approach. Indeed, degenerating to first-order or using a linear second-order scheme will enforce the flux conservation at the periodic boundaries, but then at the expense of a potential loss of accuracy or robustness. Sometimes it is also possible to apply specific exchanges through rotationally periodic boundaries. If we take the vectors \mathbf{V}_{ij} and \mathbf{V}_{ji} interpolated on one boundary and send them to override the ones interpolated on the other boundary (choosing arbitrarily one boundary over the other), then we force the conservation (but not the frame-independence). However this kind of patch is not always possible to implement in a code. It depends on its architecture, and more specifically whether it is possible or not to perform MPI communications between MUSCL reconstructions and the flux calculation. In such a case, the only way to solve the problem properly is to have a real, frame-independent vectorial interpolation method, like the one proposed in this paper.

4.3. Taylor-Green vortex

Let us now consider the case of the Taylor-Green vortex [50]. This is a classical test-case in the CFD community to assess the accuracy and performance of high-order methods. It has been considered for instance in all the editions of the International Workshop on High-Order CFD Methods [51, 52]. It consists of the direct numerical simulation of a viscous flow within a periodic cube of size $\Omega = [-\pi L, \pi L]^3$, with $L = 1 \times 10^{-3}$ m. The initial solution of velocity and pressure is given by:

$$\begin{cases} u &= V_0 \sin\left(\frac{x}{L}\right) \cos\left(\frac{y}{L}\right) \cos\left(\frac{z}{L}\right) \\ v &= -V_0 \cos\left(\frac{x}{L}\right) \sin\left(\frac{y}{L}\right) \cos\left(\frac{z}{L}\right) \\ w &= 0 \\ p &= p_0 + \frac{\rho_0 V_0^2}{16} [\cos\left(\frac{2x}{L}\right) + \cos\left(\frac{2y}{L}\right)] [\cos\left(\frac{2z}{L}\right) + 2] \end{cases}, \quad (78)$$

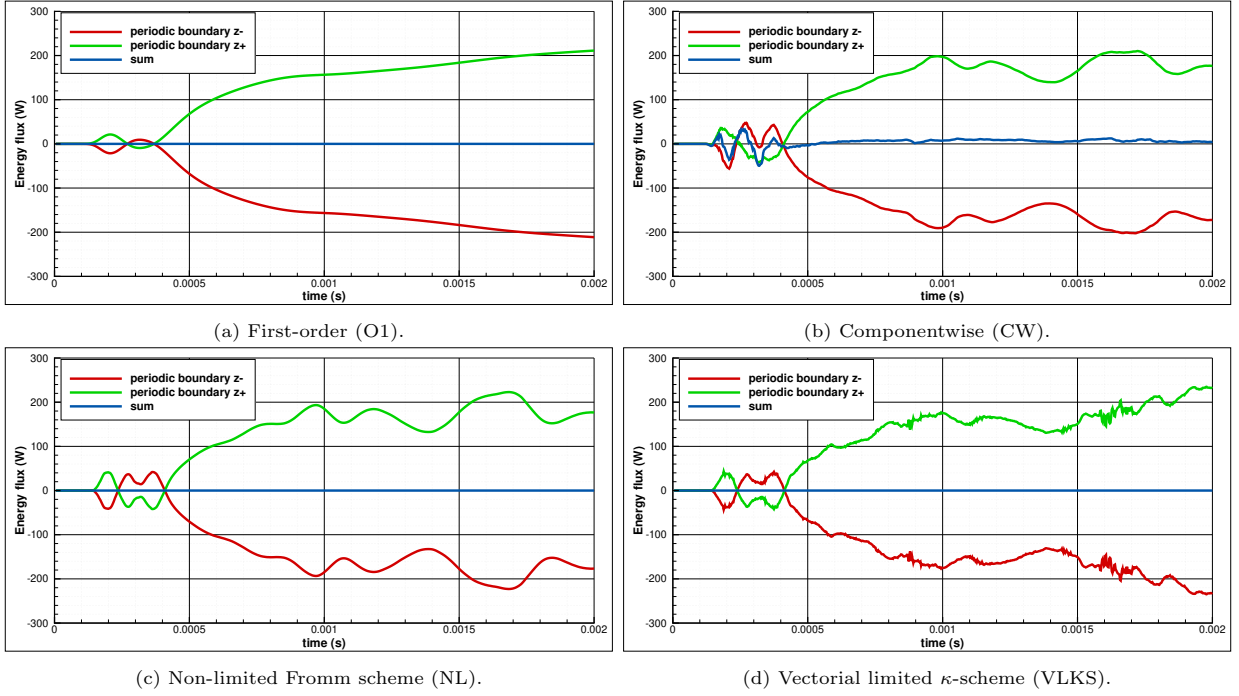


Figure 20: Total energy flux through the periodic boundaries over time (initial geometry) for the different methods.

585 with $p_0 = 1 \times 10^5$ Pa, $\rho_0 = 1.1626$ kg m $^{-3}$ and $V_0 = 34.7$ m s $^{-1}$. The physical properties are similar to those described in [51], and correspond to a temperature $T_0 = 300$ K, a Reynolds number $Re = 1600$, a Mach number $M_0 = 0.1$ and a Prandtl number $Pr = 0.71$. This flow then transitions to turbulence, with the creation of small scales, followed by a decay phase similar to decaying homogeneous turbulence (yet here non isotropic), as shown in figure 21.

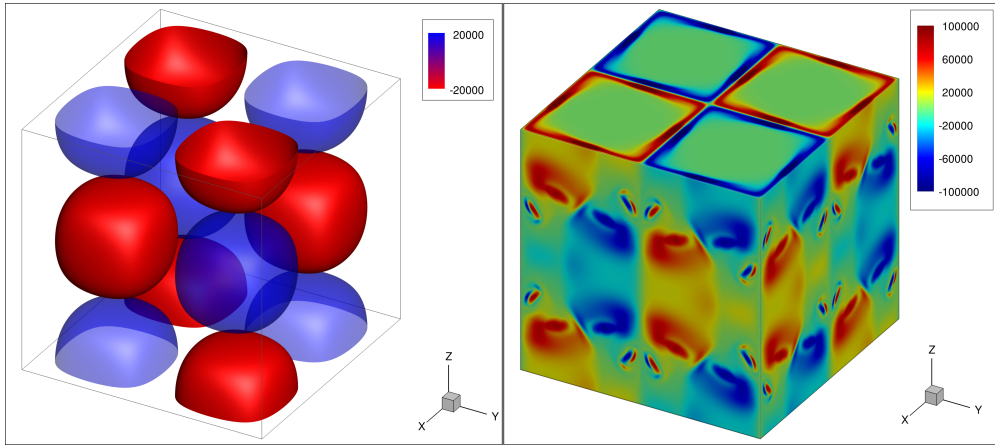


Figure 21: Z-vorticity field obtained with the VLKS method on the mesh 256^3 , at times $\bar{t} = 0$ on the left (two iso-surfaces) and $\bar{t} = 8$ on the right.

590 The objective here is to focus on the accuracy of the vectorial reconstruction. As the initial velocity field is smooth (no shock or strong shear layer involved), this means that linear second-order reconstructions for the velocity are likely to show a good stability and therefore be more accurate than any limited second-order method. However, since in real more complicated cases, limited reconstruction methods are necessary to

avoid unphysical oscillations, it is interesting to compare them in terms of accuracy on such an academic test-case. The aim is to highlight and quantify the loss of accuracy with componentwise vectorial reconstructions, compared with the VLK reconstruction introduced in section 3. As we face here a low Mach number flow, a modified version of the HLLC approximate Riemann solver is used in order to reduce the numerical dissipation in the low-Mach regime (see [53] for more details). We also consider three different cartesian grids of increasing refinement, namely with 64^3 , 128^3 and 256^3 cells.

The results obtained with the different methods on each grid are presented in figure 22 in terms of the temporal evolution of the integrated kinetic energy E_k , the kinetic energy dissipation rate $\epsilon = -\frac{dE_k}{dt}$ and the integrated enstrophy \mathcal{E} . These quantities are also non-dimensionalized as follows:

$$\overline{E_k} = \frac{E_k}{\rho_0 V_0^2}, \quad \overline{\frac{dE_k}{dt}} = \frac{dE_k}{dt} \frac{L}{\rho_0 V_0^3}, \quad \overline{\mathcal{E}} = \mathcal{E} \left(\frac{L}{V_0} \right)^2, \quad (79)$$

and plotted against a non-dimensionalized time $\bar{t} = \frac{t}{t_c}$, where $t_c = \frac{L}{V_0}$ is the convective time. This way they can be compared with reference data obtained with a spectral code. The CPU costs of each simulation are also indicated in table 3 for reference. All simulations were performed on a cluster equipped with 48-core Cascade Lake nodes, respectively using 144, 960 and 2448 cores for grids 64^3 , 128^3 and 256^3 . The increase in CPU cost with the VLKS method over a CPC method is very decent, ranging from 1% up to 9% depending on the grid refinement. With an optimized implementation, the effective cost of the VLKS method may indeed vary with the mesh resolution. With finer grids, the discrete solution is smoother overall, which means that there are fewer reconstructions that do require the full execution of the algorithm (i.e including the computation of κ_A^- or κ_B^+ to enforce the monotonicity).

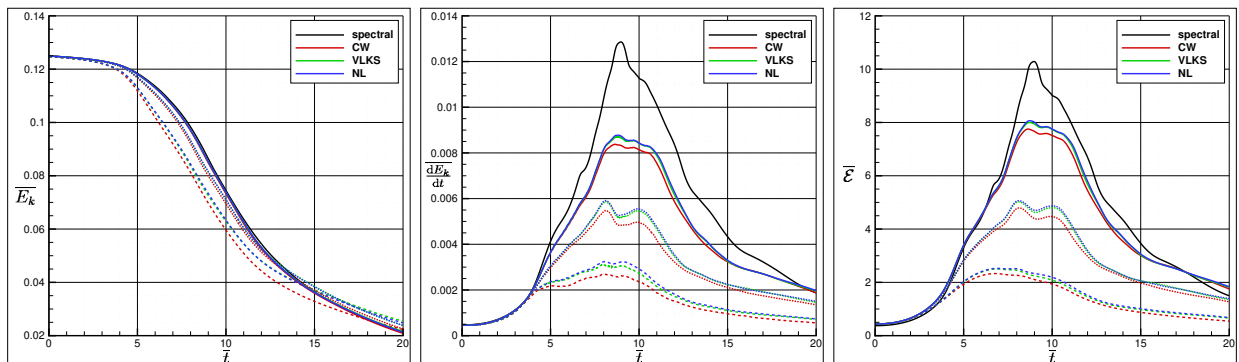


Figure 22: Temporal evolution of the integrated kinetic energy (left), kinetic energy dissipation rate (middle) and enstrophy (right), obtained with the different vectorial reconstruction methods on grids 64^3 (dashed lines), 128^3 (dotted lines) and 256^3 (solid lines).

	CW	VLKS	NL
mesh 64^3	56.40	61.66	56.20
mesh 128^3	89.83	90.81	87.19
mesh 256^3	83.72	86.08	83.56

Table 3: Taylor-Green vortex: CPU cost ($\mu\text{s}/\text{iteration}/\text{mesh cell}$).

The results shown in figure 22 demonstrate the gain of accuracy with the new VLKS method over a componentwise method. Indeed, the VLKS results are significantly closer to that obtained with the linear second-order scheme than they are to the results obtained with the componentwise method. This is especially noticeable during the time range of maximum decrease of the kinetic energy, i.e roughly between $\bar{t} = 7$ and $\bar{t} = 12$. Of course, the gain is not comparable with a switch to high-order methods, but it is still far from being negligible.

4.4. Advection of a 2D vortex

Let us now consider the advection of a vortex by an inviscid flow within a 2D periodic domain $\Omega = [-L, L]^2$, with $L = 1 \times 10^{-2}$ m. This case is described by the 2D compressible Euler equations for an ideal gas ($\gamma = 1.4$ and physical properties similar to that of air under standard conditions). The initial solution is uniform in temperature with $T_0 = 300$ K, while Gaussian velocity and pressure fields are prescribed:

$$\begin{cases} u &= u_0 - V_c \frac{y}{\sigma} \sqrt{e^{-\left(\frac{r}{\sigma}\right)^2}} \\ v &= v_0 + V_c \frac{x}{\sigma} \sqrt{e^{-\left(\frac{r}{\sigma}\right)^2}} \\ p &= p_0 \left(1 - a_0 e^{-\left(\frac{r}{\sigma}\right)^2}\right) \end{cases} . \quad (80)$$

Here $u_0 = 50 \text{ m s}^{-1}$, $v_0 = 20 \text{ m s}^{-1}$ and $p_0 = 1 \times 10^5$ Pa are the velocity components and pressure far from the vortex, $V_c = \frac{\epsilon}{\sigma}$ is the characteristic velocity of the vortex, with $\epsilon = 5 \times 10^{-3} \text{ m}^2 \text{ s}^{-1}$ its intensity and $\sigma = 1 \times 10^{-3}$ m the standard deviation of the Gaussian. Moreover, $r = \sqrt{x^2 + y^2}$ is the radius from the origin, $a_0 = \frac{1}{2} \left(\frac{V_c}{c_T}\right)^2$ stands for the maximum relative depression inside the vortex, corresponding to a maximum absolute depression of $P_0 - P_{min} = aP_0 \approx 14.04$ Pa, while $c_T = \sqrt{\frac{R}{W}T_0}$ is the isothermal speed of sound, with R the ideal gas constant and $W \approx 28.01 \text{ g mol}^{-1}$ the molar weight of air.

As in the previous test-case, the focus here is on the accuracy of the vectorial reconstruction and its impact on the quality of the solution. We use an unstructured mesh made up with approximately 26,000 triangular cells, which leads to an effective time step $\Delta t \approx 3 \times 10^{-7}$ s throughout the computation (corresponding to CFL = 2 with the SSPRK(10,4) method). Figure 23 shows the pressure field obtained with the different methods at time $t = 2$ ms, i.e after one full revolution of the vortex (5 and 2 revolutions in the x and y directions respectively), such that the exact solution at that time is given by the initial solution. The CPU cost of each method is also indicated in table 4. We can notice that the solution obtained with the CW method is polluted with first-order dispersive errors of acoustic nature, due to the false detection of extrema in the velocity components inherent to this approach. On the other hand, the solution obtained with the VLKS method is very close to the solution obtained with a linear (non-limited) second-order scheme for the velocity, which is here the closest to the exact solution. These results show that the new VLKS method entails a significant improvement in the description of acoustics over a classical componentwise approach. This is an important feature for the simulation of acoustics in real industrial applications, when non linear phenomena are also involved, requiring the use of limited reconstructions for stability. Now we have yet to assess the robustness of the VLKS method on such challenging cases that do require limiting the velocity reconstruction, and this is the purpose of the next section.

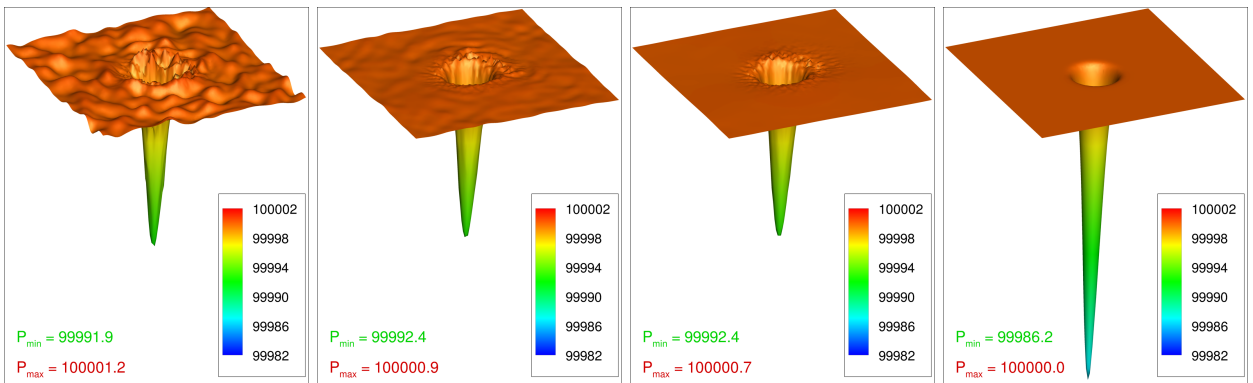


Figure 23: 3D view of the pressure field in the x - y plane for the 2D vortex advection case (pressure is shown on the z -axis) at time $t = 2$ ms. From left to right: CW, VLKS, NL and exact solution.

CW	VLKS	NL
30.48	30.00	27.33

Table 4: Advection of a 2D vortex: CPU cost ($\mu\text{s}/\text{iteration}/\text{mesh cell}$).

4.5. Liquid implosion (multi-dimensional shock tube)

In order to assess the robustness of the vectorial reconstruction methods, we finally consider a liquid
 645 implosion test case which can be seen as a multi-dimensional generalization of a classical 1D shock tube,
 as described for example in [54]. The 2D computational domain is a square of size $\Omega = [-1, 1]^2$ with solid
 walls as boundary conditions. A cartesian grid made up with 200×200 cells is projected on the domain,
 which is then rotated of an angle $\theta = \pi/4$ so that the mesh is not aligned with the reference frame (see
 figure 24). We consider the compressible barotropic Euler equations for a single-species fluid made up with
 650 liquid water. The radially symmetrical initial solution, represented in figure 24, is given by (in SI units):

$$\text{if } r \leq 0.6 \text{ then } \begin{cases} \rho &= 1000 \\ p &= 10^5 \\ v_r &= 0 \end{cases}, \quad \text{if } r > 0.6 \text{ then } \begin{cases} \rho &= 1499.95 \\ p &= 10^9 \\ v_r &= 0 \end{cases}, \quad (81)$$

with $r = \sqrt{x^2 + y^2}$ the radial coordinate and v_r the radial velocity. The following barotropic equation of
 state is used to close the system:

$$p = p_0 + c_0^2(\rho - \rho_0), \quad (82)$$

where $c_0 = (\beta_0 \rho_0)^{-1/2}$ is the constant sound speed of the liquid and $\beta_0 = 5 \times 10^{-10}$ is the isothermal
 compressibility at the reference state $\rho_0 = 1000, p_0 = 10^5$.

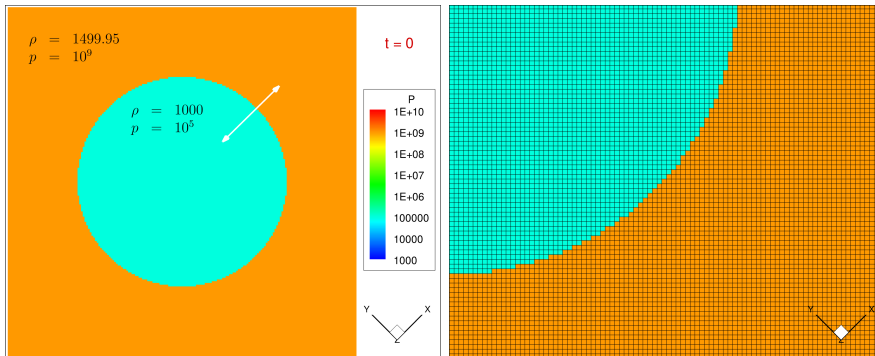


Figure 24: Pressure field for the liquid implosion test-case at $t = 0$ with the white line used to extract 1D profiles. On the
 right-hand-side: zoom on the 200×200 cartesian grid rotated with respect to the reference frame.

As explained in [54], the solution of the 2D problem can be obtained by solving the 1D Euler equations in
 655 radial coordinates, as long as the expansion and shock waves do not reach the boundaries of the square box,
 which breaks the radial symmetry. Therefore we set the computation time to $t_f = 100 \mu\text{s}$, early enough for
 the radial symmetry to still hold. This way we can extract 1D profiles at this time for the pressure, density
 and radial velocity and compare it with the exact solution, which can be obtained by solving numerically
 660 the 1D Euler equations in radial coordinates with a very fine mesh. A second-order explicit RK2 method is
 used here with a constant time step $\Delta t = 2 \times 10^{-6}$ s.

It appears from figures 25 and 26 that with the non-limited approach, the lack of monotonicity of the
 velocity reconstruction entails strong undershoots and overshoots on the pressure, which can even lead to
 a failure of the computation for a negative pressure. When using either the componentwise or the VLKS
 665 method, the solution is completely free of these undershoots and overshoots on the pressure when the most
 diffusive limiter (Minmod) is used. When using a less diffusive limiter such as the Monotonized Central,

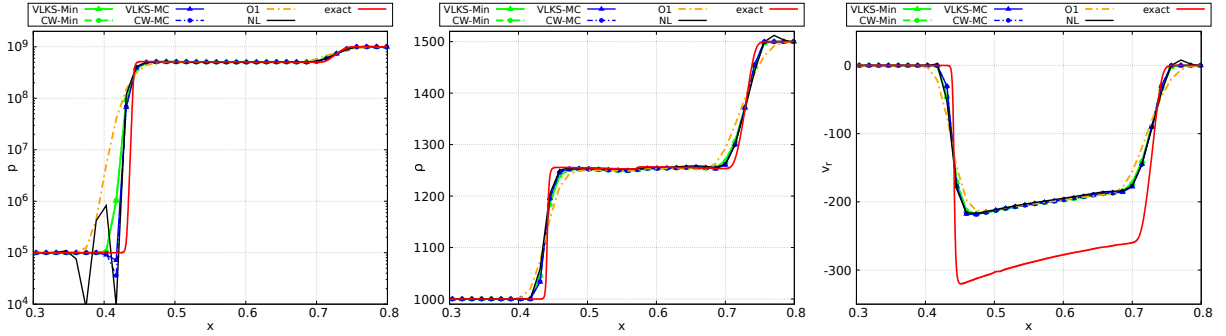


Figure 25: Comparison of several vectorial reconstruction methods for the liquid implosion test-case. Pressure, density and velocity profiles along the line of interest ($0.3 < x < 0.8$, $y = 0$) at the final time $t = 100 \mu\text{s}$.

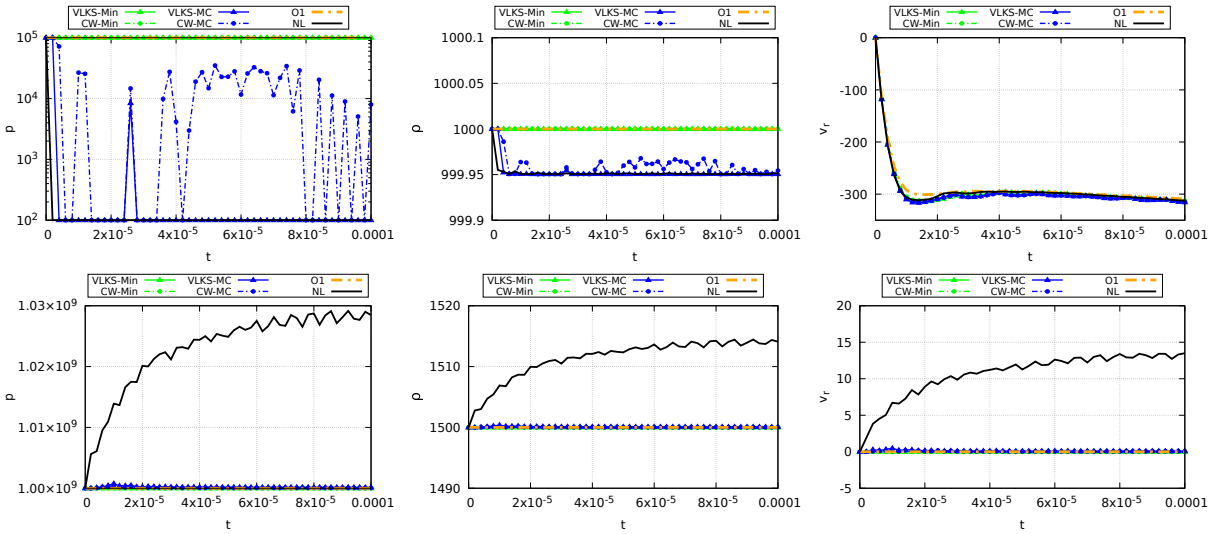


Figure 26: Minimum (first row) and maximum (second row) values over time of pressure, density and radial velocity for several vectorial reconstruction methods on the liquid implosion test-case.

both the componentwise and the VLKS methods exhibit some overshoots and undershoots on the pressure, although they are much weaker than with the linear reconstruction. This indicates that for such CFD cases, involving very strong discontinuities, with shocks and stiff equations of state, it may be necessary to use limiter functions that prioritize robustness over accuracy, such as Minmod rather than Monotonized Central (whether in scalar or vector form). The important conclusion is that, when using limiter functions with equivalent accuracy properties, the new VLKS method seems to exhibit similar robustness properties than the classical scalar componentwise approach, even on such a challenging test-case for robustness, for which a linear velocity reconstruction basically fails.

5. Conclusion

In this paper, we dealt with the reconstruction of vectorial variables in the context of finite volume multislope MUSCL methods. Until now this kind of variables were usually reconstructed using a componentwise (CW) framework, in which each vector component is treated as a scalar variable. This approach had some drawbacks since it was known to be frame-dependent and potentially leading to a loss of accuracy due to false detection of extrema. To address these issues, we first introduced in this paper an alternative formulation for the scalar case. This enabled us afterwards to introduce a new reconstruction procedure

for vectorial variables, the Vectorial Limited Kappa Scheme (VLKS) together with three Vectorial Limited Kappa (VLK) functions, namely Monotonized Central (MC), Minmod and Superbee, each one derived from their scalar counterparts. Each of these VLK functions has been tested on several numerical test-cases to assess different aspects of the limiting procedure. From these results, it comes out that the VLKS method exhibits the best behavior in terms of accuracy and robustness, while being frame-independant and with a very limited extra CPU cost compared to CW methods (not higher than 5 % on real CFD cases). More precisely, the VLKS-MC method shows a precision quite similar to a second-order linear (non-limited) method when smooth velocity gradients are involved, while exhibiting a robustness similar to CW methods for steep velocity gradients that can make non-limited methods unstable. This procedure is also quite simple to implement in a CFD code that already uses a second-order MUSCL framework, therefore we believe that it is a promising alternative to componentwise limiting functions in such codes.

Regarding perspectives, it would be interesting to perform additional numerical tests and benchmarks in order to provide a thorough assessment of vectorial reconstruction methods. One example would be a linear case with a vector field transported by a velocity field that is not divergence free, in order to see how the method handles the creation of physically admissible new extrema. Other interesting tests would be classical CFD benchmarks where the accuracy and robustness of the velocity reconstruction plays an important role, including for instance shock and rarefaction waves, or viscous and boundary layer effects. From a theoretical point of view, future work could be devoted to develop a vectorial reconstruction method for which one can prove the maximum principle on the vectorial advection equation (in the sense of the convex hull condition (37)), while still being frame-independant and providing optimal second-order accuracy.

6. Acknowledgment

This work was supported by a PhD grant from ONERA – The French Aerospace Lab. Many figures in this document have been produced with the Geogebra software [55]. The authors would like to thank P. Villedieu for valuable discussions and advice.

References

- [1] B. Van Leer, Towards the ultimate conservative difference scheme. I. The quest of monotonicity, in: H. Cabannes, R. Temam (Eds.), Proceedings of the Third International Conference on Numerical Methods in Fluid Mechanics, Lecture Notes in Physics, Springer, Berlin, Heidelberg, 1973, pp. 163–168. doi:10.1007/BFb0118673.
- [2] B. Van Leer, Towards the ultimate conservative difference scheme. II. Monotonicity and conservation combined in a second-order scheme, Journal of Computational Physics 14 (1974) 361–370. URL: <http://www.sciencedirect.com/science/article/pii/0021999174900199>. doi:10.1016/0021-9991(74)90019-9.
- [3] B. Van Leer, Towards the ultimate conservative difference scheme. III. Upstream-centered finite-difference schemes for ideal compressible flow, Journal of Computational Physics 23 (1977) 263–275. URL: <https://www.sciencedirect.com/science/article/pii/0021999177900948>. doi:10.1016/0021-9991(77)90094-8.
- [4] B. Van Leer, Towards the ultimate conservative difference scheme. IV. A new approach to numerical convection, Journal of Computational Physics 23 (1977) 276–299. URL: <https://www.sciencedirect.com/science/article/pii/002199917790095X>. doi:10.1016/0021-9991(77)90095-X.
- [5] B. Van Leer, Towards the ultimate conservative difference scheme. V. A second-order sequel to Godunov’s method, Journal of Computational Physics 32 (1979) 101–136. URL: <http://www.sciencedirect.com/science/article/pii/0021999179901451>. doi:10.1016/0021-9991(79)90145-1.
- [6] E. S. De Goes Maciel, A. P. Pimenta, N. E. Mastorakis, Comparison Among MUSCL, ENO, and WENO Procedures as Applied to Reentry Flows in 2D, Technical Report, 2014. URL: <http://wseas.us/e-library/conferences/2014/Florence/SEMOTEC/SEMOTEC-02.pdf>.
- [7] A. Harten, B. Engquist, S. Osher, S. R. Chakravarthy, Uniformly High Order Accurate Essentially Non-oscillatory Schemes, III, Journal of Computational Physics 131 (1997) 3–47. URL: <https://www.sciencedirect.com/science/article/pii/S0021999196956326>. doi:10.1006/jcph.1996.5632.
- [8] X.-D. Liu, S. Osher, T. Chan, Weighted Essentially Non-oscillatory Schemes, Journal of Computational Physics 115 (1994) 200–212. URL: <https://www.sciencedirect.com/science/article/pii/S0021999184711879>. doi:10.1006/jcph.1994.1187.
- [9] B. Cockburn, C. Johnson, C.-S. Shu, E. Tadmor, Advanced numerical approximation of nonlinear hyperbolic equations: lectures given at the 2nd session of the Centro Internazionale Matematico Estivo (C.I.M.E.) held in Cetraro, Italy, June 23-28, 1997, number 1697 in Lecture notes in mathematics, Springer, Berlin ; New York, 1998.

- [10] S. K. Godunov, I. Bohachevsky, Finite difference method for numerical computation of discontinuous solutions of the equations of fluid dynamics, *Matematičeskij sbornik* 47(89) (1959) 271–306. URL: <https://hal.archives-ouvertes.fr/hal-01620642>, publisher: Steklov Mathematical Institute of Russian Academy of Sciences.
- [11] F. Kemm, A comparative study of TVD-limiters-well-known limiters and an introduction of new ones, *Int. J. Numer. Meth. Fluids* 67 (2011) 404–440. URL: <http://doi.wiley.com/10.1002/flid.2357>. doi:10.1002/flid.2357.
- [12] N. Waterson, H. Deconinck, Design principles for bounded higher-order convection schemes – a unified approach, *Journal of Computational Physics* 224 (2007) 182–207. URL: <https://linkinghub.elsevier.com/retrieve/pii/S002199910700040X>. doi:10.1016/j.jcp.2007.01.021.
- [13] A. Harten, High resolution schemes for hyperbolic conservation laws, *Journal of Computational Physics* 49 (1983) 357–393. URL: <http://www.sciencedirect.com/science/article/pii/0021999183901365>. doi:10.1016/0021-9991(83)90136-5.
- [14] J. B. Goodman, R. J. LeVeque, On the Accuracy of Stable Schemes for 2D Scalar Conservation Laws, *Mathematics of Computation* 45 (1985) 15–21. URL: <https://www.jstor.org/stable/2008046>. doi:10.2307/2008046, publisher: American Mathematical Society.
- [15] P. Colella, Multidimensional upwind methods for hyperbolic conservation laws, *Journal of Computational Physics* 87 (1990) 171–200. URL: <http://www.sciencedirect.com/science/article/pii/002199919090233Q>. doi:10.1016/0021-9991(90)90233-Q.
- [16] S. Spekreijse, Multigrid solution of monotone second-order discretizations of hyperbolic conservation laws, *Math. Comp.* 49 (1987) 135–155. URL: <https://www.ams.org/mcom/1987-49-179/S0025-5718-1987-0890258-9/>. doi:10.1090/S0025-5718-1987-0890258-9.
- [17] A. Jameson, Analysis and Design of Numerical Schemes for Gas Dynamics, 1: Artificial Diffusion, Upwind Biasing, Limiters and their Effect on Accuracy and Multigrid Convergence, *International Journal of Computational Fluid Dynamics* 4 (1995) 171–218. URL: <https://www.tandfonline.com/doi/full/10.1080/10618569508904524>. doi:10.1080/10618569508904524.
- [18] T. Buffard, S. Clain, Monoslope and multislope MUSCL methods for unstructured meshes, *Journal of Computational Physics* (2010) 32.
- [19] T. Barth, M. Ohlberger, Finite Volume Methods: Foundation and Analysis, in: *Encyclopedia of Computational Mechanics*, American Cancer Society, 2004. URL: <https://onlinelibrary.wiley.com/doi/abs/10.1002/0470091355.ecm010>. doi:10.1002/0470091355.ecm010, section: 15 _eprint: <https://onlinelibrary.wiley.com/doi/pdf/10.1002/0470091355.ecm010>.
- [20] L. J. Durlofsky, B. Engquist, S. Osher, Triangle based adaptive stencils for the solution of hyperbolic conservation laws, *Journal of Computational Physics* 98 (1992) 64–73. URL: <https://www.sciencedirect.com/science/article/pii/002199919290173V>. doi:10.1016/0021-9991(92)90173-V.
- [21] V. Clauzon, Analyse de schémas d'ordre élevé pour les écoulements compressibles. Application à la simulation numérique d'une torche à plasma., phdthesis, Université Blaise Pascal - Clermont-Ferrand II, 2008. URL: <https://tel.archives-ouvertes.fr/tel-00235951>.
- [22] C. Le Touze, A. Murrone, H. Guillard, Multislope MUSCL method for general unstructured meshes, *Journal of Computational Physics* 284 (2015) 389–418. URL: <https://linkinghub.elsevier.com/retrieve/pii/S0021999114008493>. doi:10.1016/j.jcp.2014.12.032.
- [23] H. Xu, X. Liu, F. Li, S. Huang, C. Liu, A Novel Multislope MUSCL Scheme for Solving 2D Shallow Water Equations on Unstructured Grids, *Water* 10 (2018) 524. URL: <https://www.mdpi.com/2073-4441/10/4/524>. doi:10.3390/w10040524, number: 4 Publisher: Multidisciplinary Digital Publishing Institute.
- [24] A. Refloch, B. Courbet, A. Murrone, P. Villedieu, C. Laurent, P. Gilbank, J. Troyes, L. Tessé, G. Chaineray, J. Dargaud, E. Quémerais, F. Vuillot, CEDRE Software, Aerospace Lab (2011) p. 1–10. URL: <https://hal.archives-ouvertes.fr/hal-01182463>, publisher: Alain Appriou.
- [25] B. Courbet, C. Benoit, V. Couaillier, F. Haider, M. C. L. Pape, S. Péron, *Space Discretization Methods* (2011) 15.
- [26] G. Luttwak, J. Falcovitz, Slope limiting for vectors: A novel vector limiting algorithm, *International Journal for Numerical Methods in Fluids* 65 (2011) 1365–1375. URL: <https://onlinelibrary.wiley.com/doi/abs/10.1002/flid.2367>. doi:10.1002/flid.2367, _eprint: <https://onlinelibrary.wiley.com/doi/pdf/10.1002/flid.2367>.
- [27] G. Luttwak, J. Falcovitz, VIP (Vector Image Polygon) multi-dimensional slope limiters for scalar variables, *Computers & Fluids* 83 (2013) 90–97. URL: <https://www.sciencedirect.com/science/article/pii/S0045793012003386>. doi:10.1016/j.compfluid.2012.08.022.
- [28] G. Luttwak, On the Extension of Monotonicity to Multi-Dimensional Flows (2016) 12.
- [29] P. Hoch, E. Labourasse, A frame invariant and maximum principle enforcing second-order extension for cell-centered ALE schemes based on local convex hull preservation, *International Journal for Numerical Methods in Fluids* 76 (2014) 1043–1063. URL: <https://onlinelibrary.wiley.com/doi/abs/10.1002/flid.3969>. doi:10.1002/flid.3969, _eprint: <https://onlinelibrary.wiley.com/doi/pdf/10.1002/flid.3969>.
- [30] J. Velechovský, M. Kuchařík, R. Liska, M. Shashkov, Symmetry-preserving momentum remap for ALE hydrodynamics, *J. Phys.: Conf. Ser.* 454 (2013) 012003. URL: <https://doi.org/10.1088/1742-6596/454/1/012003>. doi:10.1088/1742-6596/454/1/012003, publisher: IOP Publishing.
- [31] P.-H. Maire, A high-order one-step sub-cell force-based discretization for cell-centered Lagrangian hydrodynamics on polygonal grids, *Computers & Fluids* 46 (2011) 341–347. URL: <https://www.sciencedirect.com/science/article/pii/S004579301000188X>. doi:10.1016/j.compfluid.2010.07.013.
- [32] P.-H. Maire, R. Loubère, P. Váchal, Staggered Lagrangian Discretization Based on Cell-Centered Riemann Solver and Associated Hydrodynamics Scheme, *Communications in Computational Physics* 10 (2011) 940–978. URL: <https://www.cambridge.org/core/journals/communications-in-computational-physics/article/abs/staggered-lagrangian-discretization-based-on-cellcentered-riemann-solver-and-associated-hydrodynamics-scheme/>

- OACF4D9038D2619C07AB249767CAE861#access-block. doi:10.4208/cicp.170310.251110a, publisher: Cambridge University Press.
- [33] I. V. Glazyrin, N. A. Mikhailov, Finite-Volume Scheme for Multicomponent Compressible Flows on Unstructured Meshes in the Focus 3D Code, *Comput. Math. and Math. Phys.* 61 (2021) 1015–1029. URL: <https://link.springer.com/10.1134/S096554252106004X>. doi:10.1134/S096554252106004X.
- [34] R. Loubère, P.-H. Maire, P. Váchal, 3D staggered Lagrangian hydrodynamics scheme with cell-centered Riemann solver-based artificial viscosity, *International Journal for Numerical Methods in Fluids* 72 (2013) 22–42. URL: <https://onlinelibrary.wiley.com/doi/abs/10.1002/flid.3730>. doi:10.1002/flid.3730, eprint: <https://onlinelibrary.wiley.com/doi/pdf/10.1002/flid.3730>.
- [35] H. Hajduk, D. Kuzmin, V. Aizinger, New directional vector limiters for discontinuous Galerkin methods, *Journal of Computational Physics* 384 (2019) 308–325. URL: <https://www.sciencedirect.com/science/article/pii/S002199911930083X>. doi:10.1016/j.jcp.2019.01.032.
- [36] H. Hajduk, D. Kuzmin, V. Aizinger, Frame-invariant directional vector limiters for discontinuous Galerkin methods (2018) 32.
- [37] X. Zeng, G. Scovazzi, A frame-invariant vector limiter for flux corrected nodal remap in arbitrary Lagrangian–Eulerian flow computations, *Journal of Computational Physics* 270 (2014) 753–783. URL: <https://www.sciencedirect.com/science/article/pii/S0021999114002411>. doi:10.1016/j.jcp.2014.03.054.
- [38] S. K. Sambasivan, M. J. Shashkov, D. E. Burton, Exploration of new limiter schemes for stress tensors in Lagrangian and ALE hydrocodes, *Computers & Fluids* 83 (2013) 98–114. URL: <https://www.sciencedirect.com/science/article/pii/S0045793012001405>. doi:10.1016/j.compfluid.2012.04.010.
- [39] S. Gottlieb, D. Ketcheson, C.-W. Shu, Strong Stability Preserving Runge-Kutta and Multistep Time Discretizations, WORLD SCIENTIFIC, 2011. URL: <http://www.worldscientific.com/worldscibooks/10.1142/7498>. doi:10.1142/7498.
- [40] P. K. Sweby, High Resolution Schemes Using Flux Limiters for Hyperbolic Conservation Laws, *SIAM J. Numer. Anal.* 21 (1984) 995–1011. URL: <http://epubs.siam.org/doi/10.1137/0721062>. doi:10.1137/0721062.
- [41] M. Berger, M. Aftosmis, S. Muman, Analysis of Slope Limiters on Irregular Grids, in: 43rd AIAA Aerospace Sciences Meeting and Exhibit, American Institute of Aeronautics and Astronautics, Reno, Nevada, 2005. URL: <http://arc.aiaa.org/doi/10.2514/6.2005-490>. doi:10.2514/6.2005-490.
- [42] D. Zhang, C. Jiang, D. Liang, L. Cheng, A review on TVD schemes and a refined flux-limiter for steady-state calculations, *Journal of Computational Physics* 302 (2015) 114–154. URL: <https://www.sciencedirect.com/science/article/pii/S0021999115005707>. doi:10.1016/j.jcp.2015.08.042.
- [43] H. Deconinck, P. L. Roe, R. Struijs, A multidimensional generalization of Roe’s flux difference splitter for the euler equations, *Computers & Fluids* 22 (1993) 215–222. URL: <https://www.sciencedirect.com/science/article/pii/S004579309390053C>. doi:10.1016/0045-7930(93)90053-C.
- [44] S. Tang, M. Li, Construction and application of several new symmetrical flux limiters for hyperbolic conservation law, *Computers & Fluids* 213 (2020) 104741. URL: <https://www.sciencedirect.com/science/article/pii/S004579302030311X>. doi:10.1016/j.compfluid.2020.104741.
- [45] B. van Leer, Upwind-difference methods for aerodynamic problems governed by the Euler equations (1985) 327–336. URL: <https://ui.adsabs.harvard.edu/abs/1985ams.conf..327V>, conference Name: Large-Scale Computations in Fluid Mechanics.
- [46] B. Koren, A robust upwind discretization method for advection, diffusion and source terms, *Numerical Methods for Advection-Diffusion Problems* (1993) 117–138. URL: <https://research.tue.nl/en/publications/a-robust-upwind-discretization-method-for-advection-diffusion-and>, publisher: Vieweg.
- [47] C. Le Touze, Geogebra applet showing the different representations of the scalar “second-order stability area”, 2022. URL: <https://www.geogebra.org/classic/ebvyvkh>.
- [48] C. Le Touze, Geogebra applet showing the vectorial “second-order stability” area, 2022. URL: <https://www.geogebra.org/classic/xwbbjr2g>.
- [49] D. I. Ketcheson, Highly Efficient Strong Stability-Preserving Runge–Kutta Methods with Low-Storage Implementations, *SIAM J. Sci. Comput.* 30 (2008) 2113–2136. URL: <http://epubs.siam.org/doi/10.1137/07070485X>. doi:10.1137/07070485X.
- [50] G. I. Taylor, A. E. Green, Mechanism of the Production of Small Eddies from Large Ones, *Proceedings of the Royal Society of London Series A* 158 (1937) 499–521. URL: <https://ui.adsabs.harvard.edu/abs/1937RSPSA.158..499T>. doi:10.1098/rspa.1937.0036, aDS Bibcode: 1937RSPSA.158..499T.
- [51] K. Hillewaert, Problem C3.5 Direct numerical simulation of the Taylor-Green vortex at Re=1600, 2011. URL: https://cfd.ku.edu/hiocfd/case_c3.5.pdf.
- [52] K. Hillewaert, BS1 - DNS of the transition of the Taylor-Green vortex, Re=1600, 2016. URL: https://how4.cenaero.be/system/files/filedepot/12/BS1_Summary_Hillewaert.pdf.
- [53] C. Le Touze, N. Rutard, Numerical methods for diffuse interface multifluid models, in: ECCOMAS 2022-8th European Congress on Computational Methods in Applied Sciences and Engineering, 2022.
- [54] E. F. Toro, Multidimensional Test Problems, in: E. F. Toro (Ed.), *Riemann Solvers and Numerical Methods for Fluid Dynamics: A Practical Introduction*, Springer, Berlin, Heidelberg, 2009, pp. 585–596. URL: https://doi.org/10.1007/b79761_17. doi:10.1007/b79761_17.
- [55] Geogebra, 2023. URL: <https://www.geogebra.org>.

Appendix A. Illustration of the frame-dependence of componentwise vectorial reconstructions

The issue with componentwise vectorial reconstructions, described in section 2.4, is illustrated here with an example. Let us consider three square cells K_1, K_2, K_3 in a 2D cartesian mesh with a length equal to 1 (see Figure A.27), in which three vectors are defined using the basis $\mathcal{B} = \{\mathbf{e}_x, \mathbf{e}_y\}$:

$$\mathbf{V}_1 = \begin{pmatrix} 0 \\ 1 \end{pmatrix}, \quad \mathbf{V}_2 = \begin{pmatrix} 1 \\ 1 \end{pmatrix}, \quad \mathbf{V}_3 = \begin{pmatrix} 0 \\ 2 \end{pmatrix}. \quad (\text{A.1})$$

865 The reconstruction $\mathbf{V}_{2+1/2}$ on the face delimiting K_2 and K_3 is computed with a componentwise approach, with the following slopes and their ratio:

$$p_x^+ = -1, \quad p_x^- = 1, \quad r_x = -1, \quad p_y^+ = 1, \quad p_y^- = 0, \quad r_y = 0. \quad (\text{A.2})$$

As the slope limiting function vanishes when the slope ratio $r \leq 0$, then the reconstruction degenerates to first-order for both components, which gives

$$\mathbf{V}_{2+1/2} = \begin{pmatrix} \mathbf{V}_{2,x} + \frac{\varphi(r_x)p_x^+}{2} \\ \mathbf{V}_{2,y} + \frac{\varphi(r_y)p_y^+}{2} \end{pmatrix} = \mathbf{V}_2 = \begin{pmatrix} 1 \\ 1 \end{pmatrix}. \quad (\text{A.3})$$

870 Let us now consider the basis \mathcal{B}' , obtained by a rotation of an angle $\pi/3$ of the basis \mathcal{B} , that is with a rotation matrix $\mathbf{R}_{-\pi/3}$ that reads:

$$\mathbf{R}_{-\pi/3} = \begin{pmatrix} \cos\left(-\frac{\pi}{3}\right) & -\sin\left(-\frac{\pi}{3}\right) \\ \sin\left(-\frac{\pi}{3}\right) & \cos\left(-\frac{\pi}{3}\right) \end{pmatrix}. \quad (\text{A.4})$$

In this new basis, vectors are thus determined by $\mathbf{V}'_i = \mathbf{R}_{-\pi/3} \mathbf{V}_i$ for $i = 1, 2, 3$, which gives:

$$\mathbf{V}'_1 = \begin{pmatrix} \frac{\sqrt{3}}{2} \\ \frac{1}{2} \end{pmatrix}, \quad \mathbf{V}'_2 = \begin{pmatrix} \frac{1+\sqrt{3}}{2} \\ \frac{1-\sqrt{3}}{2} \end{pmatrix}, \quad \mathbf{V}'_3 = \begin{pmatrix} \sqrt{3} \\ 1 \end{pmatrix}, \quad (\text{A.5})$$

as well as:

$$p_x'^+ = \frac{\sqrt{3}-1}{2}, \quad p_x'^- = \frac{1}{2}, \quad r_x' = \frac{1}{\sqrt{3}-1}, \quad p_y'^+ = \frac{1+\sqrt{3}}{2}, \quad p_y'^- = -\frac{\sqrt{3}}{2}, \quad r_y' = -\frac{\sqrt{3}}{1+\sqrt{3}}. \quad (\text{A.6})$$

Thus we have a first-order reconstruction for the y component as $r_y' < 0$, but a second-order reconstruction for the x component as $r_x' > 0$. More precisely, we get:

$$\mathbf{V}'_{2+1/2} = \begin{pmatrix} \mathbf{V}'_{2,x} + \frac{1}{2}\varphi(r_x')p_x'^+ \\ \mathbf{V}'_{2,y} + \frac{1}{2}\varphi(r_y')p_y'^+ \end{pmatrix} = \mathbf{V}'_2 + \begin{pmatrix} \frac{\sqrt{3}-1}{4}\varphi\left(\frac{1}{\sqrt{3}-1}\right) \\ 0 \end{pmatrix} = \mathbf{V}'_2 + p'_x \mathbf{e}_x, \quad (\text{A.7})$$

875 with $p'_x > 0$ for any limiting function φ satisfying (14). Theoretically, a frame-invariant method should give identical reconstructed vectors whatever basis chosen, so we should have:

$$\mathbf{V}'_{2+1/2} = \mathbf{R}_{-\pi/3} \mathbf{V}_{2+1/2}. \quad (\text{A.8})$$

This is not the case in the present example, as we have:

$$\mathbf{V}'_{2+1/2} = \mathbf{V}'_2 + p'_x \mathbf{e}_x = \mathbf{R}_{-\pi/3} \mathbf{V}_2 + p'_x \mathbf{e}_x = \mathbf{R}_{-\pi/3} \mathbf{V}_{2+1/2} + p'_x \mathbf{e}_x \neq \mathbf{R}_{-\pi/3} \mathbf{V}_{2+1/2}. \quad (\text{A.9})$$

This illustrates the frame-dependence of the componentwise reconstruction.

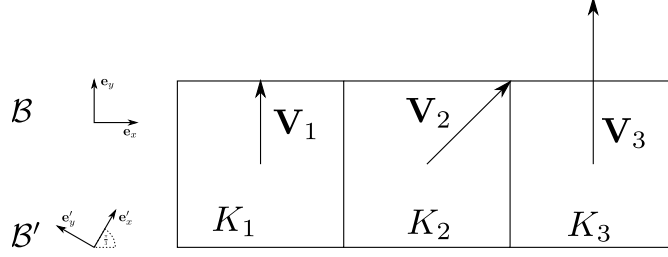


Figure A.27: Illustration of the frame-dependence of componentwise vectorial reconstructions.

880 Appendix B. Proofs of section 2.4

As already mentioned in section 2.4, let us begin by noticing that, whether the vectorial quantities to be reconstructed are initially defined in a 2D or 3D space, the reconstruction procedure can always be tackled in the 2D plane generated by the slope vectors \mathbf{p}_{ij}^- and \mathbf{p}_{ij}^+ . So in any case it is possible to work with 2D slope vectors \mathbf{p}_{ij}^- and \mathbf{p}_{ij}^+ , which are potentially a projection in this plane. By extension, it is also possible to consider 3D vectors with two components in this plane and a third vanishing component, which will be useful for the proofs below. For the sake of conciseness, we also drop below the indices ij for the slopes.

Theorem 1. *If slopes are colinear, then we have the only totally frame-independent componentwise reconstruction.*

Proof. As slopes are colinear, there exists a scalar α such that $\mathbf{p}^- = \alpha\mathbf{p}^+$, so any component k is reconstructed with a limiter function $\varphi(p_k^-/p_k^+) = \varphi(\alpha)$. And since α is frame-invariant, the slope limiting function, as well as the reconstruction, are also frame-invariant. \square

Theorem 2. *If slopes are noncolinear and $\mathbf{p}^+ \cdot \mathbf{p}^- > 0$, then for any basis, there is always at least one component reconstructed at second-order accuracy.*

Proof. If we develop the scalar product, we get $\sum_{k=1}^d p_k^+ p_k^-$. For this sum to be positive, we need to have at least one product $p_k^+ p_k^-$ positive, which means that at least one component has a ratio $r_k > 0$ and therefore a non-vanishing limiter. \square

Theorem 3. *If slopes are noncolinear and $\mathbf{p}^+ \cdot \mathbf{p}^- > 0$, then there exists at least one basis in which at least one component is first-order accurate.*

Proof. Let us consider for example the 3D basis $\mathcal{B} = \{\mathbf{e}_1, \mathbf{e}_2, \mathbf{e}_3\}$ with:

$$\mathbf{e}_1 = \frac{\mathbf{p}^+ + \mathbf{p}^-}{\|\mathbf{p}^+ + \mathbf{p}^-\|}, \quad \mathbf{e}_2 = \frac{\mathbf{p}^+ \wedge \mathbf{p}^-}{\|\mathbf{p}^+ \wedge \mathbf{p}^-\|}, \quad \mathbf{e}_3 = \frac{\mathbf{e}_1 \wedge \mathbf{e}_2}{\|\mathbf{e}_1 \wedge \mathbf{e}_2\|}, \quad (\text{B.1})$$

such that the second component of the slopes vanishes in this basis. Then we get for the third component of the slopes:

$$(p_3^+)^{\mathcal{B}} = \mathbf{p}^+ \cdot \mathbf{e}_3 = \frac{\|\mathbf{p}^+\|^2 \|\mathbf{p}^-\|^2 - (\mathbf{p}^+ \cdot \mathbf{p}^-)^2}{\|\mathbf{e}_1 \wedge \mathbf{e}_2\|} = -\mathbf{p}^- \cdot \mathbf{e}_3 = -(p_3^-)^{\mathcal{B}}, \quad (\text{B.2})$$

which means that $r_3 = -1$ for the slopes ratio and therefore the limiter vanishes. Thus, a componentwise reconstruction will have at least one component reconstructed at first-order in this basis. \square

Theorem 4. *If slopes are noncolinear and $\mathbf{p}^+ \cdot \mathbf{p}^- > 0$, then there exists at least one basis in which all components are second-order accurate.*

Proof. Let us consider for example the basis $\mathcal{B} = \{\mathbf{e}_1, \mathbf{e}_2, \mathbf{e}_3\}$ with

$$\begin{aligned} \mathbf{e}_1 &= \frac{\mathbf{p}^- - \epsilon \mathbf{p}^+}{\|\mathbf{p}^- - \epsilon \mathbf{p}^+\|}, & \mathbf{e}_2 &= \frac{\mathbf{p}^+ \wedge \mathbf{p}^-}{\|\mathbf{p}^+ \wedge \mathbf{p}^-\|}, \\ \mathbf{e}_3 &= \frac{\mathbf{e}_1 \wedge \mathbf{e}_2}{\|\mathbf{e}_1 \wedge \mathbf{e}_2\|} = \frac{\|\mathbf{p}^-\|^2 \mathbf{p}^+ + \epsilon \|\mathbf{p}^+\|^2 \mathbf{p}^- - (\mathbf{p}^+ \cdot \mathbf{p}^-)(\mathbf{p}^- + \epsilon \mathbf{p}^+)}{\|\mathbf{p}^- - \epsilon \mathbf{p}^+\| \|\mathbf{p}^+ \wedge \mathbf{p}^-\|}, \end{aligned} \quad (\text{B.3})$$

and ϵ a positive scalar. The second component of the slopes vanishing in this basis, let us compute the first and third components of both slopes. For the first component we get

$$\mathbf{p}^+ \cdot \mathbf{e}_1 = \frac{(\mathbf{p}^+ \cdot \mathbf{p}^-) - \epsilon \|\mathbf{p}^+\|^2}{\|\mathbf{p}^- - \epsilon \mathbf{p}^+\|}, \quad \mathbf{p}^- \cdot \mathbf{e}_1 = \frac{\|\mathbf{p}^-\|^2 - \epsilon (\mathbf{p}^+ \cdot \mathbf{p}^-)}{\|\mathbf{p}^- - \epsilon \mathbf{p}^+\|}. \quad (\text{B.4})$$

For any ϵ such that

$$0 < \epsilon \leq \min \left(\frac{\|\mathbf{p}^-\|^2}{\mathbf{p}^+ \cdot \mathbf{p}^-}, \frac{\mathbf{p}^+ \cdot \mathbf{p}^-}{\|\mathbf{p}^+\|^2} \right), \quad (\text{B.5})$$

910 then the first component of both slopes is positive, so is their ratio, and therefore the first component is reconstructed with a second-order accuracy. Now for the third component, we have

$$\mathbf{p}^- \cdot \mathbf{e}_3 = \epsilon \frac{\|\mathbf{p}^-\|^2 \|\mathbf{p}^+\|^2 - (\mathbf{p}^+ \cdot \mathbf{p}^-)^2}{\|\mathbf{p}^- - \epsilon \mathbf{p}^+\| \|\mathbf{p}^+ \wedge \mathbf{p}^-\|} = \epsilon (\mathbf{p}^+ \cdot \mathbf{e}_3). \quad (\text{B.6})$$

Hence we get $r_3 = \epsilon$ for the slope ratio, the limiting function is non-vanishing, and the third component is also reconstructed with a second-order accuracy. \square

Theorem 5. *If slopes are noncolinear and $\mathbf{p}^+ \cdot \mathbf{p}^- < 0$, then for any basis, there is always at least one component reconstructed at first-order accuracy.* 915

Proof. For the scalar product $\sum_{k=1}^d p_k^+ p_k^-$ to be negative, we need to have at least one product $p_k^+ p_k^-$ negative. The limiting function therefore vanishes for this component, which leads to a first-order accurate reconstruction. \square

Theorem 6. *If slopes are noncolinear and $\mathbf{p}^+ \cdot \mathbf{p}^- < 0$, then there exists at least one basis in which at least one component is second-order accurate.* 920

Proof. Let us consider for example the basis $\mathcal{B} = \{\mathbf{e}_1, \mathbf{e}_2, \mathbf{e}_3\}$ with:

$$\mathbf{e}_1 = \frac{\mathbf{p}^+ - \mathbf{p}^-}{\|\mathbf{p}^+ - \mathbf{p}^-\|}, \quad \mathbf{e}_2 = \frac{\mathbf{p}^+ \wedge \mathbf{p}^-}{\|\mathbf{p}^+ \wedge \mathbf{p}^-\|}, \quad \mathbf{e}_3 = \frac{\mathbf{e}_1 \wedge \mathbf{e}_2}{\|\mathbf{e}_1 \wedge \mathbf{e}_2\|}, \quad (\text{B.7})$$

such that the second component of the slopes vanishes in this basis. Then we get for the third component of the slopes:

$$\mathbf{p}^- \cdot \mathbf{e}_3 = \frac{(\mathbf{p}^+ \cdot \mathbf{p}^-) - \|\mathbf{p}^+\|^2 \|\mathbf{p}^-\|^2}{\|\mathbf{p}^+ - \mathbf{p}^-\| \|\mathbf{p}^+ \wedge \mathbf{p}^-\|} = \mathbf{p}^+ \cdot \mathbf{e}_3, \quad (\text{B.8})$$

which means that $r_3 = 1$ for the slopes ratio, the limiter returns $\varphi(1) = 1$ and therefore the reconstruction is second-order accurate for this component. \square 925

Theorem 7. *If slopes are noncolinear and $\mathbf{p}^+ \cdot \mathbf{p}^- < 0$, then there exists at least one basis in which all components are first-order accurate.*

Proof. Let us consider for example the basis $\mathcal{B} = \{\mathbf{e}_1, \mathbf{e}_2, \mathbf{e}_3\}$ with

$$\begin{aligned} \mathbf{e}_1 &= \frac{\mathbf{p}^- + \epsilon \mathbf{p}^+}{\|\mathbf{p}^- + \epsilon \mathbf{p}^+\|}, & \mathbf{e}_2 &= \frac{\mathbf{p}^+ \wedge \mathbf{p}^-}{\|\mathbf{p}^+ \wedge \mathbf{p}^-\|}, \\ \mathbf{e}_3 &= \frac{\mathbf{e}_1 \wedge \mathbf{e}_2}{\|\mathbf{e}_1 \wedge \mathbf{e}_2\|} = \frac{(\mathbf{p}^+ \cdot \mathbf{p}^-)(\epsilon \mathbf{p}^+ - \mathbf{p}^-) + \|\mathbf{p}^-\|^2 \mathbf{p}^+ - \epsilon \|\mathbf{p}^+\|^2 \mathbf{p}^-}{\|\mathbf{p}^- + \epsilon \mathbf{p}^+\| \|\mathbf{p}^+ \wedge \mathbf{p}^-\|}, \end{aligned} \quad (\text{B.9})$$

and ϵ a positive scalar. The second component of the slopes vanishing in this basis, let us compute the first and third components of both slopes. For the first component we get

$$\mathbf{p}^+ \cdot \mathbf{e}_1 = \frac{(\mathbf{p}^+ \cdot \mathbf{p}^-) + \epsilon \|\mathbf{p}^+\|^2}{\|\mathbf{p}^- + \epsilon \mathbf{p}^+\|}, \quad \mathbf{p}^- \cdot \mathbf{e}_1 = \frac{\|\mathbf{p}^-\|^2 + \epsilon(\mathbf{p}^+ \cdot \mathbf{p}^-)}{\|\mathbf{p}^- + \epsilon \mathbf{p}^+\|}. \quad (\text{B.10})$$

For any ϵ such that

$$0 < \epsilon \leq \min \left(-\frac{\|\mathbf{p}^-\|^2}{\mathbf{p}^+ \cdot \mathbf{p}^-}, -\frac{\mathbf{p}^+ \cdot \mathbf{p}^-}{\|\mathbf{p}\|^2} \right), \quad \text{or} \quad \epsilon \geq \max \left(-\frac{\|\mathbf{p}^-\|^2}{\mathbf{p}^+ \cdot \mathbf{p}^-}, -\frac{\mathbf{p}^+ \cdot \mathbf{p}^-}{\|\mathbf{p}\|^2} \right) > 0, \quad (\text{B.11})$$

then the first components of both slopes \mathbf{p}^+ and \mathbf{p}^- have opposite signs. Their ratio is therefore negative and the first component is reconstructed with a first-order accuracy. Then we get for the third component of the slopes:

$$\mathbf{p}^- \cdot \mathbf{e}_3 = \epsilon \frac{(\mathbf{p}^+ \cdot \mathbf{p}^-)^2 - \|\mathbf{p}^-\|^2 \|\mathbf{p}^+\|^2}{\|\mathbf{p}^- - \epsilon \mathbf{p}^+\| \|\mathbf{p}^+ \wedge \mathbf{p}^-\|} = -\epsilon (\mathbf{p}^+ \cdot \mathbf{e}_3). \quad (\text{B.12})$$

Hence the slope ratio r_3 is negative, the limiting function vanishes, and the third component is also reconstructed with a first-order accuracy. \square

Theorem 8. *If slopes are noncolinear and $\mathbf{p}^+ \cdot \mathbf{p}^- = 0$, then for all orthonormal basis \mathcal{B}_0 with at least one component colinear with one of the vectorial slopes, all components will be reconstructed with a first-order accuracy.*

Proof. Let say that \mathbf{p}^+ is colinear with the component \mathbf{e}_1 of $\mathcal{B}_0 = \{\mathbf{e}_1, \mathbf{e}_2, \mathbf{e}_3\}$. Then the components of \mathbf{p}^+ corresponding to \mathbf{e}_2 and \mathbf{e}_3 vanish, leading to a first-order reconstruction for these two components. When the other slope \mathbf{p}^- is projected on \mathbf{e}_1 , then we get 0 for this slope on this component, leading to a first-order accurate reconstruction too. \square

Theorem 9. *If slopes are noncolinear and $\mathbf{p}^+ \cdot \mathbf{p}^- = 0$, for any basis different from \mathcal{B}_0 as defined in the precedent theorem, there is always one component reconstructed with a second-order accuracy and one component reconstructed with a first-order accuracy.*

Proof. We prove it by contradiction. Let us suppose that there exists a basis $\mathcal{B} = \{\mathbf{e}'_1, \mathbf{e}'_2, \mathbf{e}'_3\}$ such that all components are reconstructed with a second order accuracy, that is to say

$$\forall i \in \{1, 2, 3\}, \quad \langle \mathbf{p}^+ \cdot \mathbf{e}'_i \rangle \langle \mathbf{p}^- \cdot \mathbf{e}'_i \rangle > 0. \quad (\text{B.13})$$

Then there is a contradiction with the fact that the scalar product has to be zero, as we have :

$$\mathbf{p}^+ \cdot \mathbf{p}^- = \sum_{i=1}^3 \langle \mathbf{p}^+ \cdot \mathbf{e}'_i \rangle \langle \mathbf{p}^- \cdot \mathbf{e}'_i \rangle = 0. \quad (\text{B.14})$$

Hence, there is always at least one component nonpositive, and it is impossible to get all components reconstructed with a second-order accuracy. Let us say now that there is an orthonormal basis $\mathcal{B} = \{\mathbf{e}'_1, \mathbf{e}'_2, \mathbf{e}'_3\}$, different from \mathcal{B}_0 as defined in the previous theorem, and such that the slope ratio is nonpositive for all components. Then, the scalar product in this basis writes:

$$\mathbf{p}^+ \cdot \mathbf{p}^- = \sum_{i=1}^3 \langle \mathbf{p}^+ \cdot \mathbf{e}'_i \rangle \langle \mathbf{p}^- \cdot \mathbf{e}'_i \rangle. \quad (\text{B.15})$$

As this scalar product is zero, and because the slope ratio in this basis is nonpositive for each component, it follows:

$$\forall i \in \{1, 2, 3\}, \quad \langle \mathbf{p}^+ \cdot \mathbf{e}'_i \rangle = 0 \quad \text{or} \quad \langle \mathbf{p}^- \cdot \mathbf{e}'_i \rangle = 0. \quad (\text{B.16})$$

As the basis \mathcal{B} is orthonormal, we can't have a situation such that all components are zero for the same slope, so there exists at least one component \mathbf{e}'_i and one component \mathbf{e}'_j such that

$$\mathbf{e}'_i \cdot \mathbf{p}^+ = 0, \quad \text{and} \quad \mathbf{e}'_j \cdot \mathbf{p}^- = 0 \quad (\text{B.17})$$

As \mathbf{e}'_i is orthogonal with \mathbf{p}^+ , it belongs to the plane spanned by the basis $\{\mathbf{p}^-, \mathbf{p}^+ \wedge \mathbf{p}^-\}$. So there exists two scalar α and β such that :

$$\mathbf{e}'_i = \alpha \mathbf{p}^- + \beta \mathbf{p}^+ \wedge \mathbf{p}^-. \quad (\text{B.18})$$

960 With similar ideas, there exists $\tilde{\alpha}$ and $\tilde{\beta}$ such that :

$$\mathbf{e}'_j = \tilde{\alpha} \mathbf{p}^+ + \tilde{\beta} \mathbf{p}^+ \wedge \mathbf{p}^-. \quad (\text{B.19})$$

As these two vectors are orthonormal, their scalar product has to be zero:

$$\mathbf{e}'_i \cdot \mathbf{e}'_j = \beta \tilde{\beta} \mathbf{p}^+ \wedge \mathbf{p}^- = 0, \quad (\text{B.20})$$

965 meaning that $\beta = 0$ or $\tilde{\beta} = 0$. However, it means that at least one of the component of the basis \mathcal{B} is colinear with one of the two slopes, which is a contradiction with its definition. Hence, there is no basis different from \mathcal{B}_0 as defined in the previous theorem such that all components are reconstructed with a first-order accuracy. \square

Appendix C. Limiter function formalism for vectorial reconstructions

Appendix C.1. Introducing vectorial limiter functions as complex numbers

As explained in section 3.2, the effective slope \mathbf{p}_{ij} is a convex combination of the forward and backward slopes \mathbf{p}_{ij}^+ and \mathbf{p}_{ij}^- (see relation (40)). Except in the trivial case of colinear slopes, this implies that \mathbf{p}_{ij} belongs to $\mathcal{P}_{ij} = \mathcal{P}(\mathbf{p}_{ij}^+, \mathbf{p}_{ij}^-)$, the 2-dimensional plane generated by the slope vectors, whether \mathbf{V}_i is defined in a 2- or 3-dimensional space. It is thus possible to identify this 2-dimensional plane with the complex plane. To do this, we introduce the function F which associates a vector \mathbf{V} in the plane \mathcal{P}_{ij} with its corresponding point of affix \tilde{V} in the complex plane:

$$F : \mathbf{V} \in \mathcal{P}_{ij} \rightarrow \tilde{V} \in \mathbb{C}. \quad (\text{C.1})$$

Hence, if we introduce

$$\tilde{p}_{ij} = F(\mathbf{p}_{ij}), \quad \tilde{p}_{ij}^+ = F(\mathbf{p}_{ij}^+), \quad \tilde{p}_{ij}^- = F(\mathbf{p}_{ij}^-), \quad (\text{C.2})$$

975 it is possible to write the effective slope in its complex form:

$$\tilde{p}_{ij} = \frac{1 + \kappa_{ij}}{2} \tilde{p}_{ij}^+ + \frac{1 - \kappa_{ij}}{2} \tilde{p}_{ij}^- = \tilde{p}_{ij}^+ \tilde{\varphi}_{ij}, \quad (\text{C.3})$$

with

$$\tilde{\varphi}_{ij} = \tilde{\varphi}(\tilde{r}_{ij}) = \frac{1 + \kappa_{ij}}{2} + \frac{1 - \kappa_{ij}}{2} \tilde{r}_{ij}, \quad \tilde{r}_{ij} = \frac{\tilde{p}_{ij}^-}{\tilde{p}_{ij}^+}. \quad (\text{C.4})$$

Hence the slopes ratio does have a definition in the vectorial case. It is the complex number \tilde{r}_{ij} that describes the similarity transformation between the complex slopes \tilde{p}_{ij}^+ and \tilde{p}_{ij}^- . In the same way, $\tilde{\varphi}_{ij}$ defines the similarity transformation between \tilde{p}_{ij}^+ and the effective slope \tilde{p}_{ij} . This is illustrated in figure C.28 with \tilde{p}_{ij}^+ placed on the real axis of the complex plane by convention. We also introduce the following notations to stand for the modulus and argument of \tilde{r}_{ij} and $\tilde{\varphi}_{ij}$:

$$\begin{aligned} R_{ij} &\triangleq |\tilde{r}_{ij}| & ; & \quad \theta_{ij} \triangleq \arg(\tilde{r}_{ij}) \\ \Phi_{ij} &\triangleq |\tilde{\varphi}_{ij}| & ; & \quad \phi_{ij} \triangleq \arg(\tilde{\varphi}_{ij}) \end{aligned} \quad (\text{C.5})$$

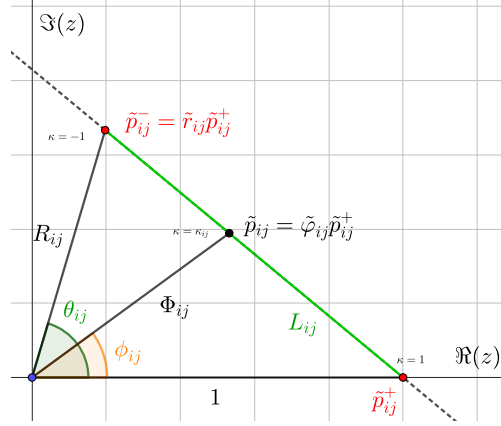


Figure C.28: A vectorial limiter function represented in the complex plane.

These complex notations being introduced, it is now possible to translate the bounding of $\|\mathbf{V}_{ij} - \mathbf{V}_i\|$ described by (44) as a bounding on $|\tilde{V}_{ij} - \tilde{V}_i|$, and then as a condition on the modulus Φ_{ij} :

$$\Phi_{ij} \leq \sigma_{ij} \min \left[\max(1, R_{ij}), \min(\eta_{ij}^- R_{ij}, \eta_{ij}^+) \right], \quad (\text{C.6})$$

985 i.e a condition similar to the one established for the scalar case (15). From the second-order condition in (44), it is also possible to define a minimum bound on Φ_{ij} , which is actually the modulus Φ_{ij}^{Min} of the vectorial Minmod limiter (cf relation (C.14) below), exactly as the scalar Minmod limiter represents the lower bound of φ in the scalar case (cf relation (15)). The vectorial "second-order monotonicity area" is thus defined in terms of the modulus of the limiter function by

$$\Phi_{ij}^{Min} \leq \Phi_{ij} \leq \sigma_{ij} \min \left[\max(1, R_{ij}), \min(\eta_{ij}^- R_{ij}, \eta_{ij}^+) \right]. \quad (\text{C.7})$$

990 As it stands, the bounding on Φ_{ij} is not yet equivalent to the vectorial "second-order monotonicity area" defined in (44), we still have to add some constraint on the argument ϕ_{ij} . Actually, since the point \tilde{V}_{ij} has to lie on the line $(\tilde{V}_{ij}^-, \tilde{V}_{ij}^+)$ due to the second-order condition, then ϕ_{ij} is geometrically linked to Φ_{ij} and we just need to express this relation. After a few lines of calculation with the areas of triangles $(\tilde{V}_i, \tilde{V}_{ij}^-, \tilde{V}_{ij}^+)$ and $(\tilde{V}_i, \tilde{V}_{ij}^-, \tilde{V}_{ij})$ and $(\tilde{V}_i, \tilde{V}_{ij}^+, \tilde{V}_{ij})$, it comes the following relation (for $0 < \phi_{ij} \leq \theta_{ij} < \frac{\pi}{2}$):

$$\Phi_{ij}(\phi_{ij}, R_{ij}, \theta_{ij}) = \frac{R_{ij} \sin \theta_{ij}}{R_{ij} \sin(\theta_{ij} - \phi_{ij}) + \sin \phi_{ij}}. \quad (\text{C.8})$$

995 From this relation, we can now express ϕ_{ij} as a function of Φ_{ij} , R_{ij} and θ_{ij} . Using the relation $\sin(a - b) = \sin a \cos b - \sin b \cos a$, we can show that $\sin \phi_{ij}$ is the solution of a second-order polynomial equation, describing the intersection of the circle of radius Φ_{ij} with the line $(\tilde{V}_{ij}^-, \tilde{V}_{ij}^+)$. We can also show that its discriminant is non-negative, and thus we have two real solutions (potentially equal), reading:

$$\sin \phi_{ij} = R_{ij} \sin \theta_{ij} \frac{1 - R_{ij} \cos \theta_{ij} \pm [(\Phi_{ij} L_{ij})^2 - (R_{ij} \sin \theta_{ij})^2]^{1/2}}{\Phi_{ij} L_{ij}^2}, \quad (\text{C.9})$$

with L_{ij} given by (52). Finally, solutions for the argument ϕ_{ij} are:

$$\left\{ \begin{array}{l} \phi_{ij}(\Phi_{ij}, R_{ij}, \theta_{ij}) = \arcsin \left(R_{ij} \sin \theta_{ij} \frac{1 - R_{ij} \cos \theta_{ij} \pm [(\Phi_{ij} L_{ij})^2 - (R_{ij} \sin \theta_{ij})^2]^{1/2}}{\Phi_{ij} L_{ij}^2} \right) \\ 0 \leq \phi_{ij} \leq \theta_{ij} \leq \frac{\pi}{2} \end{array} \right. . \quad (\text{C.10})$$

Thus, any complex limiter $\tilde{\varphi}_{ij}$ satisfying (C.7) for its modulus Φ_{ij} , and whose argument ϕ_{ij} is given by relation (C.10), belongs to the vectorial "second-order monotonicity area".

Appendix C.2. Connection with the VLK formulation

As in the scalar case, there is a strict equivalence between the vectorial limiter formulation and the VLK formulation introduced in section 3. Indeed, the coefficient κ_{ij} can be written as a function of \tilde{r}_{ij} and $\tilde{\varphi}_{ij}$, which reads:

$$\kappa_{ij}(\tilde{r}_{ij}, \tilde{\varphi}_{ij}) = \kappa_{ij}(R_{ij}, \theta_{ij}, \Phi_{ij}, \phi_{ij}) = 1 - 2 \left(\frac{1 + \Phi_{ij}^2 - 2\Phi_{ij} \cos \phi_{ij}}{1 + R_{ij}^2 - 2R_{ij} \cos \theta_{ij}} \right)^{1/2} = 1 - 2 \frac{F_{ij}}{L_{ij}}, \quad (\text{C.11})$$

with

$$F_{ij} = \sqrt{1 + \Phi_{ij}^2 - 2\Phi_{ij} \cos \phi_{ij}} = \frac{\|\mathbf{V}_{ij}^+ - \mathbf{V}_{ij}\|}{\|\mathbf{V}_{ij}^+ - \mathbf{V}_i\|} = \frac{\|\mathbf{p}_{ij}^+ - \mathbf{p}_{ij}\|}{\|\mathbf{p}_{ij}^+\|}, \quad (\text{C.12})$$

representing the length of the segment $[\mathbf{V}_{ij}, \mathbf{V}_{ij}^+]$ normalised by that of $[\mathbf{V}_i, \mathbf{V}_{ij}^+]$. For $0 < \phi_{ij} \leq \theta_{ij} < \frac{\pi}{2}$, we can also write:

$$\kappa_{ij}(R_{ij}, \theta_{ij}, \Phi_{ij}, \phi_{ij}) = 1 - \frac{2 \sin \phi_{ij}}{R_{ij} \sin(\theta_{ij} - \phi_{ij}) + \sin \phi_{ij}}. \quad (\text{C.13})$$

These formulas are the vectorial equivalent of relation (22), giving κ_{ij} as a function of r_{ij} and φ_{ij} in the scalar case.

Appendix C.3. Vectorial limiter functions

According to the framework described above, it is possible to express the VLK functions introduced in section 3.4 in the form of vectorial (complex) limiter functions. But in general this does not provide a more practical framework for implementation than VLK functions, because the corresponding formulas for Φ_{ij} and ϕ_{ij} can be quite heavy. Let's still do the exercise here for the vectorial Minmod limiter, whose expression is quite simple. If we write $\tilde{\varphi}_{ij}^{Min}$ and $\tilde{\varphi}_{ij}^H$ the points in the complex plane which respectively stand for the vectorial Minmod limiter and the intersection between the altitude from \tilde{V}_i and the line $(\tilde{V}_{ij}^-, \tilde{V}_{ij}^+)$, then we get:

$$\phi_{ij}^{Min}(\tilde{r}_{ij}) = \max[0, \min(\phi_{ij}^H, \theta_{ij})], \quad \Phi_{ij}^{Min}(\tilde{r}_{ij}) = \begin{cases} \Phi_{ij}^H & \text{if } \max(\alpha_{ij}, \beta_{ij}) \leq \frac{\pi}{2} \\ \min(1, R_{ij}) & \text{else} \end{cases}, \quad (\text{C.14})$$

where Φ_{ij}^H and ϕ_{ij}^H are the modulus and argument of $\tilde{\varphi}_{ij}^H$, that read:

$$\Phi_{ij}^H = \frac{R_{ij} \sin \theta_{ij}}{L_{ij}}, \quad \phi_{ij}^H = \arccos \Phi_{ij}^H. \quad (\text{C.15})$$

Note that the vectorial Minmod limiter reduces to the scalar Minmod limiter when slopes are colinear and in the same direction. Indeed, we get in that case $\max(\alpha_{ij}, \beta_{ij}) = \pi$ and thus $\Phi_{ij}^{Min} = \min(R_{ij}, 1)$, which is the scalar Minmod limiter.

Appendix C.4. Reducing to the scalar case

Actually, we can show that the whole vectorial framework introduced in this paper reduces to the classical multislope scalar method when the slopes vectors are colinear. If they are in the same direction, i.e if $\theta_{ij} = 0$ (no local extremum), then we have $R_{ij} = r_{ij} > 0$ and $\phi_{ij} = 0$, as well as:

$$L_{ij}^2 = 1 + R_{ij}^2 - 2R_{ij} = (1 - R_{ij})^2 = (1 - r_{ij})^2, \quad (\text{C.16})$$

and:

$$\kappa_{ij} = 1 - 2 \left[\frac{(1 - \Phi_{ij})^2}{(1 - R_{ij})^2} \right]^{1/2} = 1 - 2 \frac{1 - \varphi_{ij}}{1 - r_{ij}}, \quad (\text{C.17})$$

which is the formula (22) established for the scalar case. Now if the triangle $(\tilde{V}_{ij}^-, \tilde{V}_i, \tilde{V}_{ij}^+)$ is flat in \tilde{V}_{ij}^- , i.e when $\alpha_{ij} = \pi$ and $\beta_{ij} = 0$, it comes $\|\mathbf{p}_{ij}^-\| < \|\mathbf{p}_{ij}^+\|$, hence $r_{ij} < 1$ and we get $L_{ij} = 1 - r_{ij}$. Regarding the bounding values for κ_{ij} derived in section 3.3, it comes:

$$\left\{ \begin{array}{l} \kappa_A^- = \frac{R_{ij}^2 - 1 + 2R_{ij}\eta_{ij}^- L_{ij}}{L_{ij}^2} = \frac{2\eta_{ij}^- r_{ij} - 1 - r_{ij}}{1 - r_{ij}} = \kappa^-(r_{ij}, \eta_{ij}^-) \\ \kappa_B^- = \frac{R_{ij}^2 - 1 - 2R_{ij}\eta_{ij}^- L_{ij}}{L_{ij}^2} = \frac{-2\eta_{ij}^- r_{ij} - 1 - r_{ij}}{1 - r_{ij}} \\ \kappa_A^+ = \frac{R_{ij}^2 - 1 + 2\eta_{ij}^+ L_{ij}}{L_{ij}^2} = \frac{2\eta_{ij}^+ - 1 - r_{ij}}{1 - r_{ij}} = \kappa^+(r_{ij}, \eta_{ij}^-) \\ \kappa_B^+ = \frac{R_{ij}^2 - 1 - 2\eta_{ij}^+ L_{ij}}{L_{ij}^2} = \frac{-2\eta_{ij}^+ - 1 - r_{ij}}{1 - r_{ij}} \end{array} \right. \quad (\text{C.18})$$

1030 On the other hand, if the triangle $(\tilde{V}_{ij}^-, \tilde{V}_i, \tilde{V}_{ij}^+)$ is flat in \tilde{V}_{ij}^+ , i.e when $\alpha_{ij} = 0$ and $\beta_{ij} = \pi$, it comes $\|\mathbf{p}_{ij}^-\| > \|\mathbf{p}_{ij}^+\|$, hence $r_{ij} > 1$ and we get $L_{ij} = r_{ij} - 1$. The bounding values for κ_{ij} then read:

$$\left\{ \begin{array}{l} \kappa_A^- = \frac{R_{ij}^2 - 1 + 2R_{ij}\eta_{ij}^- L_{ij}}{L_{ij}^2} = \frac{-2\eta_{ij}^- r_{ij} - 1 - r_{ij}}{1 - r_{ij}} \\ \kappa_B^- = \frac{R_{ij}^2 - 1 - 2R_{ij}\eta_{ij}^- L_{ij}}{L_{ij}^2} = \frac{2\eta_{ij}^- r_{ij} - 1 - r_{ij}}{1 - r_{ij}} = \kappa^-(r_{ij}, \eta_{ij}^-) \\ \kappa_A^+ = \frac{R_{ij}^2 - 1 + 2\eta_{ij}^+ L_{ij}}{L_{ij}^2} = \frac{-2\eta_{ij}^+ - 1 - r_{ij}}{1 - r_{ij}} \\ \kappa_B^+ = \frac{R_{ij}^2 - 1 - 2\eta_{ij}^+ L_{ij}}{L_{ij}^2} = \frac{2\eta_{ij}^+ - 1 - r_{ij}}{1 - r_{ij}} = \kappa^+(r_{ij}, \eta_{ij}^-) \end{array} \right. \quad (\text{C.19})$$

We get back the relations (25) obtained in the scalar case for $\kappa^-(r_{ij}, \eta_{ij}^-)$ and $\kappa^+(r_{ij}, \eta_{ij}^+)$. More precisely κ_A^- and κ_A^+ , correspond respectively to κ^- and κ^+ when $r_{ij} < 1$, and κ_B^- and κ_B^+ correspond respectively to κ^- and κ^+ when $r_{ij} > 1$. In the case $\|\mathbf{p}_{ij}^-\| = \|\mathbf{p}_{ij}^+\|$, i.e when $r_{ij} = R_{ij} = 1$, then we have $L_{ij} = 0$ and the bounding values for κ_{ij} are not defined, which means that all reconstructions are equivalent. Finally, if the slopes \mathbf{p}_{ij}^- and \mathbf{p}_{ij}^+ are colinear but in opposite directions, i.e when $\theta_{ij} = \pi$, then we have a local extremum with $r_{ij} = -R_{ij} < 0$. In this case, we get $\sigma_{ij} = 0$ and the reconstruction is first-order accurate, exactly like in the scalar case.